Vacuum Ultraviolet Fourier-transform Spectroscopy of ^{16}O and ^{18}O

K.-F. Lai[1], D. Manalili[1], W. Ubachs[1], R. Cooke[2], M. Pettini[3], N. de Oliveira[4], and E. J. Salumbides[1,5]

[1] Department of Physics and Astronomy, LaserLaB, Vrije Universiteit De Boelelaan 1081, 1081 HV Amsterdam, The Netherlands
[2] Centre for Extragalactic Astronomy, Durham University, South Road, Durham DH1 3LE, UK
[3] Institute of Astronomy, University of Cambridge, Madingley Road, Cambridge CB3 0HA, UK
[4] Synchrotron Soleil, Orme des Merisiers, St. Aubin, BP 48, 91192 Gif sur Yvette Cedex, France; e.j.salumbides@vu.nl

Abstract

A spectroscopic study of atomic oxygen (O I) is performed using the Fourier-transform vacuum ultraviolet (VUV) spectrometer at the Dichroïsme Et Spectroscopie par Interaction avec le Rayonnement Synchrotron beamline of the SOLEIL synchrotron. Transition frequencies of O I lines in the range between 76,000 and 151,000 cm^{-1}, corresponding to wavelengths between 665 and 1306 Å, are presented. In the wavelength window a data set of 208 lines is obtained for which line centers were determined at an accuracy of $\leqslant 0.035$ cm^{-1}, verified through a comparison with previous VUV-laser spectroscopy at an accuracy of 0.008 cm^{-1}. Transitions to upper states belonging to several ns and nd Rydberg series that converge to the ^{4}S$_{3/2}$, ^{2}D, and ^{2}P ionization limits are presented. Besides studies on the main ^{16}O isotope, measurements of the ^{18}O isotope are also performed, for which an enriched sample of ^{18}O$_2$ gas is used. A least-squares optimization analysis is performed after merging the present new data set with some relevant accurate literature data to extract a list of level energies at high accuracy. When comparing with the database of the National Institute of Standards and Technology, good agreement is found for levels with low principal quantum numbers $n \leqslant 7$ or below excitation energies of 108,000 cm^{-1}; however, significant deviations were found for levels with $n > 7$. The main result of the present study is the realization of an improved data set of transition frequencies and level energies for O I, with its usefulness demonstrated in a comparison with high-resolution astronomical spectra showing absorption in the line of sight to distant quasars.

Unified Astronomy Thesaurus concepts: Atomic spectroscopy (2099)

1. Introduction

Oxygen is the third-most abundant element in the universe and is almost entirely produced in massive stars that end their lives as core-collapse supernovae. As a consequence of its high cosmological abundance, oxygen is commonly observed in stars, galaxies, and gas clouds and, more generally, is often considered the main tracer of element production through stellar nucleosynthesis, referred to as metallicity in the astronomical community. Neutral oxygen in atomic form has been detected spectroscopically in the interstellar medium of the Milky Way (Hébrard & Moos 2003), in supernovae (Taubenberger et al. 2013), in the Jovian atmosphere (Brown 1981), in the Martian atmosphere (Stewart et al. 1992), in comets (McKay et al. 2012), and in our own atmosphere (Conway et al. 1988).

At large cosmological distances, neutral gas clouds are usually observed in absorption against the light of unrelated background quasars (Wolfe et al. 2005). Such systems offer an astrophysical laboratory to study oxygen. First, in clouds that have been least enriched by stellar nucleosynthesis, the O I absorption lines are intrinsically narrow (Cooke et al. 2015), allowing a detailed study of the line profiles. Moreover, the oxygen abundance can be measured to an accuracy of $\lesssim 5\%$. Second, charge transfer reactions ensure that oxygen is predominantly neutral and accurately traces the neutral

hydrogen (H I) atoms (Field & Steigman 1971). Therefore, the ratio O I/H I is almost equivalent to the intrinsic O/H ratio. Charge transfer also ensures that oxygen accurately traces deuterium (Savin 2002; Cooke & Pettini 2016).

As part of a survey to discover new examples of the most metal-poor gas clouds that exhibit neutral deuterium (D I) absorption (Cooke et al. 2014), two clouds were discovered that also display absorption to higher-n O I Rydberg states; these are also referred to as high-order transitions. While O I absorption lines are commonly observed in metal-poor gas clouds, it is uncommon to simultaneously observe such high-order lines in D I and O I absorption near the H I Lyman limit. In these two cases, the O I absorption lines appeared to be shifted relative to their expected locations as listed in the Atomic Spectra Database of the National Institute of Standards and Technology (NIST; Kramida et al. 2020), using the wavelengths of the D I absorption lines as a reference. This NIST line list is, for the vacuum ultraviolet (VUV) lines probing high-n levels, based on Moore's tables (Moore 1993), which are again based on original studies by Huffmann et al. (1967a, 1967b) that were conducted more than 50 years ago. The relative shifts observed are as large as $\Delta\lambda/\lambda \sim 6 \times 10^{-5}$, significantly larger than the 3×10^{-6} fitting uncertainty of astronomical line positions. The laboratory wavelengths of the D I absorption lines are known to very high accuracy, and they confirm that the wavelength calibration of the astronomical observations is accurate, suggesting that the discrepancy might stem from the O I reference lines. This realization motivated us to reinvestigate the O I absorption spectrum at high precision in the VUV wavelength range.

As for the laboratory measurements, the pioneering work of Runge and Paschen (1896, 1897, 1898) in the 1890s resulted in

---

[5] Corresponding author.

the first classification of the atomic oxygen spectrum. The spectroscopic investigations of Hopfield (1924, 1931) in the 1920s extended the observed range into the ultraviolet, where the O I spectral series and splittings could be used to confront calculations from contemporary developments in quantum theory. Edlén compiled and extended these classical emission studies into a monograph (Edlén 1943), which was later improved, expanded and reported in a series of papers by Eriksson and Isberg (Eriksson & Isberg 1963, 1964; Eriksson 1965; Eriksson & Isberg 1968; Isberg 1968). Herzberg also included the principal lines of oxygen in the list of atomic standards that he measured in connection to his determination of the Lamb shift in helium (Herzberg 1958). The absorption measurements by Huffman et al. (1967a, 1967b) resulted in a comprehensive data set including Rydberg series converging to the first ionization limit with transitions originating from the ground ^3P as well as metastable ^1D and ^1S states. In the latter study an absolute uncertainty of the wavelength calibration of around 0.002 nm or 2 cm^{-1} was estimated.

Ivanov et al. (2008) measured Doppler-free VUV O I spectra with narrowband harmonic-upconverted laser sources in the wavelength range 94–103 nm with estimated uncertainties of 0.008 cm^{-1}. Two-photon Doppler-free spectroscopy with a narrowband 226 nm laser source was employed by Marinov et al. (2017) to reach $3p$ ^3P states with uncertainties estimated at 0.0019 cm^{-1}. In these high-resolution laser spectroscopic studies the fine structure of some excited levels could be resolved. The fine-structure splittings in the $2p^4$ ^3P ground state have been measured at high accuracy for all three natural isotopes ^{16}O, ^{17}O, and ^{18}O (Zink et al. 1991; Brown et al. 1993; De Natale et al. 1993). The classical studies of Parker & Holmes (1953) have also determined the ^{18}O isotope shifts, while more recent laser spectroscopic studies focusing on the isotope shifts include Marin et al. (1993), Ernst et al. (1989), and Gianfrani et al. (1990).

Currently the most accurate compilation for the ultraviolet lines of O I is that reported by Civiš et al. (2018). While their measurements were performed in the near- and mid-infrared wavelength ranges, they have combined all of the accurate information from the studies mentioned above (Eriksson & Isberg 1963, 1968; Isberg 1968; Lurie & Baird 1986; Brown et al. 1987; Chang et al. 1988; Ivanov et al. 2008; Marinov et al. 2017).

Here we report accurate measurements obtained from VUV Fourier-transform spectroscopy (FTS) using a synchrotron radiation source. More than 200 transitions are accurately measured, where those involving levels of principal quantum number $n > 5$ are considerably improved, with important consequences for the use of these lines as calibration standards in astronomical observations. The measurements have been performed for both ^{16}O and ^{18}O species.

2. Experimental

Atomic oxygen is generated using two different methods to dissociate molecular oxygen: (1) by a DC electric discharge, and (2) by producing an oxygen plasma inside the gas filter in the Dichroïsme Et Spectroscopie par Interaction avec le Rayonnement Synchrotron (DESIRS). Spectra were recorded from natural O_2 gas and isotopically $^{18}O_2$-enriched oxygen gas (Cambridge Isotopes). From our spectral recordings it was deduced that the enriched sample contained a 88% ^{18}O composition.

2.1. DC Discharge Source

The DC discharge cell used is located downstream of the DESIRS beamline, at about 0.5 m distance from the Fourier-transform (FT) instrument housed inside the gas sample chamber of the FT spectroscopy branch (de Oliveira et al. 2016). The discharge source is similar to the one used by Western et al. (2020), except that the discharge cell in the present study is windowless in order to access the far VUV spectral range. The distance between anode and cathode measures 20 cm. A stable flow of a mixture of O_2 gas and He carrier gas is maintained through the discharge cell via the inlet port and is extracted through the capillary outlet ports of the windowless cell into the main vacuum chamber, which is evacuated by a 1500 liter s^{-1} turbo pump. A second stage of differential pumping based upon two 300 liter s^{-1} ionic pumps guarantees the base pressure for the opening of the two valves isolating the FTS gas sample chamber (de Oliveira et al. 2016). The oxygen plasma is generated between the cathode and the anode of a DC electric discharge at a voltage difference of around 1 kV with a stabilized discharge current of 20 mA. The discharge is further stabilized by optimizing the pressure and by mixing in of helium carrier gas, at a He:O_2 admixture of about 3:1, where the maximum total pressure is constrained by the capacity of the differential pumping system. In order to stabilize and sustain the discharge also some amounts of neon or argon gas were added to the mixture.

2.2. Gas Spectral Filter

Isotopic shift measurements were performed by introducing O_2 gas into a windowless gas filter, located close to the undulator upstream of the DESIRS beamline. This filter is usually filled with noble gas for the purpose of suppressing the high-energy harmonics produced in the undulator (Mercier et al. 2000). The use of the gas filter for the production of atoms and measuring their VUV absorption was recently explored for N atoms (Lai et al. 2020). The gas density is not measured, and the absorbing column length is not exactly known, but the gas flow rate through the inlet is controlled in order to optimize signal strength. The maximum pressure is limited by the set point of the safety shutters that automatically block the beamline. The gas filter can be visually monitored through a viewing window where characteristic plasma emission can be observed tracing the synchrotron pencil beam, as shown in Figure 1. In the absorbing gas column, the synchrotron beam and its harmonics induce the photodissociation and photo-ionization of molecular oxygen leading to plasma generation. Oxygen atoms are produced in the ground state, as well as in the metastable states. The glow seen in Figure 1 is predominantly caused by fluorescence in the decay from the higher-lying metastable state $2p^4$ $^1S_0$ to the lower-lying metastable $2p^4$ $^1D_2$ state. The absorption spectra of the oxygen plasma are measured by the FT instrument some 17 m further downstream in the beamline. Only the first three members of the principal line series are recorded as transitions to higher-lying levels are not sufficiently strong. Samples of the abundant $^{16}O_2$, as well as enriched $^{18}O_2$ isotopes were used to measure and disentangle the isotopic line shifts of O I.

2.3. VUV Fourier-transform Spectrometer

The DESIRS beamline of the SOLEIL Synchrotron facility is equipped with a high-resolution VUV Fourier-transform
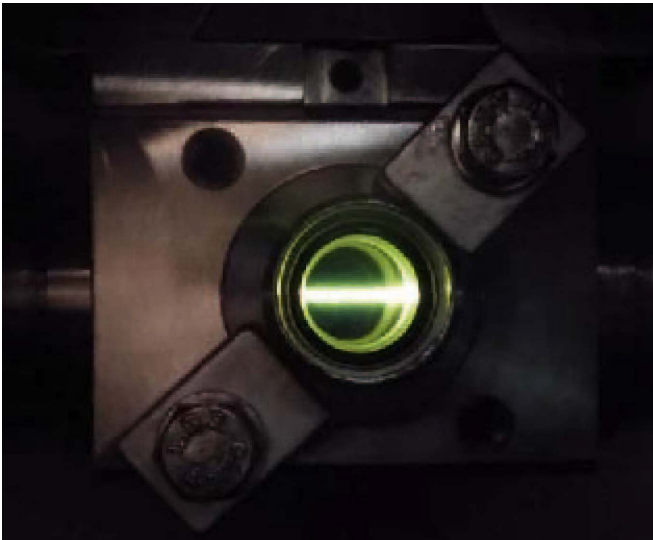
Figure 1. Oxygen glow from the gas filter (one of two methods for O I production) where the synchrotron beam is passing. The bright fluorescence at 5577 Å corresponds to the emission between the $2p^4$ metastable states $^1S_0$ and $^1D_2$, the same line that gives the characteristic green color of auroral glows.

Figure 2. Comparison of spectra between the present FTS measurements and the high-precision laser spectroscopy measurements of Ivanov et al. (2008), validating the uncertainty of the absolute frequency scale of the VUV spectrometer to be within 0.01 cm^{-1} in the present work.

Figure 3. Comparison of the deconvoluted Gaussian line width component for transitions below the (^4S) O II limit under the different experimental conditions of discharge and gas filter. The temperature of the O I atoms for both experimental conditions is extracted via a linear relationship and setting a fixed zero intercept at the origin.

spectrometer (VUV-FTS), which was described in detail previously (de Oliveira et al. 2011, 2016). The crucial innovation of this unique VUV-FTS instrument is the exploitation of wave front division interferometry for generating an interferogram avoiding transmission through beam splitters as seen in conventional FTS. The absorbing gas volume is located between the source and the VUV interferometer, allowing for a geometric arrangement where the absorption may occur at some distance from the VUV-FTS.

2.4. Frequency Calibration

The frequency (or wavelength) calibration of the FT interferometer is intrinsically related to the VUV optical path difference, which is measured via interferometric detection of the fringes of a HeNe laser probing the back surface of the moving reflector (de Oliveira et al. 2011). The FT spectroscopy frequency scale is strictly linear and, in principle, requires a single reference if precise absolute calibration is needed. The wavelength calibration is verified and improved by interpolation of measured lines from the VUV-laser study by Ivanov et al. (2008). This comparison, represented in Figure 2, shows that the final absolute accuracy of the VUV-FTS is accurate to within 0.01 cm^{-1} (at 1σ). The accuracy of the present measurements of O I lines, taking into account their signal-to-noise ratio, their line width, and the statistical averaging from multiple spectra is estimated at 0.035 cm^{-1}. All frequencies and level energies in the present study, given in units of cm^{-1}, relate to vacuum wave numbers.

2.5. Line Widths

The observed line widths of the transitions range between 0.4 and 0.9 cm^{-1} and include several contributions. A part is due to the instrumental line width of the VUV-FTS, which is determined by the travel length of the interferometer arm amounting to 0.27 cm^{-1} for the entire frequency coverage of the O I measurements. The transition line widths with the instrumental contribution taken out by deconvolution is plotted as a function of transition frequency in Figure 3. The Doppler
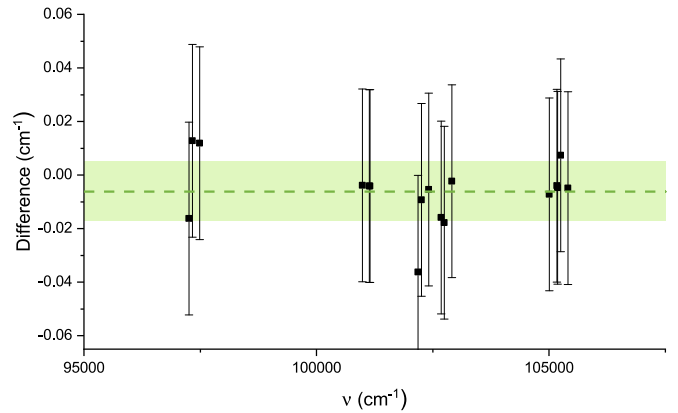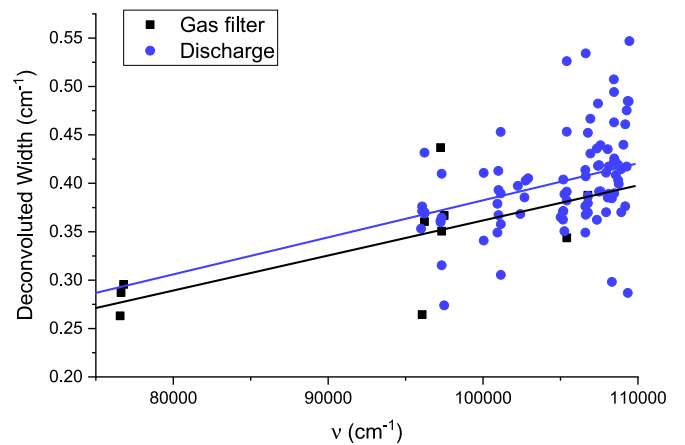
broadening gives a significant contribution, which scales with the square root of the temperature of oxygen atoms and scales linearly with increasing transition frequencies. For example, at room temperature for transition frequencies of 100,000 cm^{-1} the Doppler width is 0.31 cm^{-1}. In Figure 3, the line widths are indicated separately for those data points obtained using the gas spectral filter and those with the discharge source. An effective temperature can be extracted from the slope of a linear fit, which yields a temperature of 420 K for the gas filter. Under discharge conditions the temperature is expected to be larger than for the gas filter, and therewith the Doppler broadening as observed by the steeper slope for the discharge data set in Figure 3 that yields a temperature of 490 K. On the other hand, the intercept of the linear fit gives an underlying line width that is independent of transition frequency (hence independent of the Doppler effect). For the gas filter and discharge subset below the limit, a linear fit yields an intercept close to zero (and fixed to zero in Figure 3 to extract the slope). When a separate linear fit was performed for the discharge subset above the first ionization limit where both the slope and intercept were free parameters, the intercept obtained was slightly above zero leading to an additional line width contribution of 0.11(5) cm^{-1}, which hints toward an effect of autoionization. This
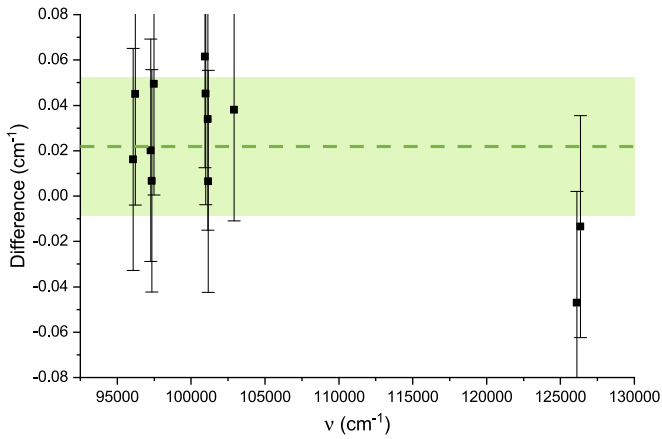
Figure 4. Comparison of transition frequency between discharge and gas filter condition to validate the potential DC Stark shift during discharge.

effect glimpsed in the aggregate is seen in striking examples that show substantial broadening due to autoionization as discussed below. Significant broadening for transitions to $4d'$ $^3S_1$ and $4d'$ $^3D_3$ is observed, in marked contrast to sharp transitions for $4d'$ ^3P_J where autoionization is forbidden under the LS-coupling approximation.

2.6. Assessment of Stark Effects

Within the discharge environment, the 50 V cm^{-1} potential across the electrodes may lead to possible DC Stark shifts. The charges from the plasma in principle also give rise to Stark shifts, but with the low densities in the setup this effect is expected to be much smaller. The DC Stark shifts can be estimated from the differential quantum defects of the levels involved in the transition in similar fashion to Zimmerman et al. (1979). The quantum defects for each level are extracted by comparing the level energies to a hydrogenic case, where we have taken the Rydberg limit of O I from the experimentally determined value of 109 837.02 cm^{-1} (Kramida et al. 2020).

The transitions observed in this study belong to the $l = 0, 2$ or s, d series. For the s series, the interaction with the p levels is taken to be the dominant one that gives rise to the polarizability and in turn the DC Stark shift. For the d series, interactions with the p and f levels are taken into account. When no level energies for p or f states are available, we extrapolate the trend from those at lower n. For transitions to principal quantum number $n < 8$, the DC Stark shift is estimated to be below 0.001 cm^{-1}. For Rydberg states this effect is larger, and for the highest principal $n = 17$ in this study a conservative estimate for the DC Stark shift is ± 0.02 cm^{-1}. These are all within the final uncertainty that is specified for the transition energies.

Recordings of transitions involving the $3s$, $4s$, and $5s$ states using the gas spectral filter as well as the discharge do not show differences in the line positions as plotted in Figure 4, confirming the expectation that the DC Stark shifts are below the experimental uncertainties. The lower oscillator strength to higher $n > 5$ states prohibits the observation with the gas spectral filter; thus a similar comparison is not possible. Nevertheless, the observed line widths of the transitions to higher-lying n levels can be used to put an upper bound to the DC Stark shifts. For a given n, the $l = \pm (n - 1)$ components have the largest shifts but in opposite directions; hence a broadening is expected for higher n and a slight shift in the position of the line center of gravity. Such an additional

n-dependent broadening contribution is not observed, which supports the conservative estimate discussed above.

3. Results

3.1. Observed Spectra

FT spectra were recorded from 76,000 to 151,000 cm^{-1}, which covers the range from the 131 nm principal O I transition to the highest O II ionization limit at 66.5 nm. A portion of the VUV FT spectrum for the range 108,000–109,800 cm^{-1} is shown in Figure 5 with the sharp features assigned to atomic oxygen lines. The spectrum illustrates the difficulty of analyzing the features in view of the fact that the atomic O I lines are overlaid by broader molecular features in the discharge. The strong broad absorptions in this region belong to O_2 ionization resonances (Keller-Rudek et al. 2013). Moreover, band signatures with narrow lines from stable diatomic molecules are also visible. The main contaminant is N_2 as a result of ambient gas leaking into the system. This gives rise to strong dipole-allowed N_2 absorption bands, clearly identified at 108,300 cm^{-1}, 108,700 cm^{-1}, and 109,500 cm^{-1}. A weak CO signature is also present near 109,450 cm^{-1}. These molecular signatures present in Figure 5 do not prohibitively interfere with the positions of the O I lines and do not prevent its analysis.

A second VUV FT overview spectrum for the range 133,000–136,600 cm^{-1} is displayed in Figure 6. This spectrum covers the O I ns' and nd' Rydberg series converging to the higher-lying ^2D state in O II, and originating from the ^3P ground state. All the O I transitions in this range originating from the ^3P ground-state probe resonances above the first $(^4S_{3/2})$ ionization limit and should therefore be subject to autoionization. However, the O I lines observed do not show broadening due to rapid ionization, at least not at the scale of the line width of the VUV-FTS instrument used.

In addition, spectra are displayed that show some characteristic features in the VUV spectrum of O I. In Figure 7 the strongest principal resonance line of oxygen at 1302 Å is shown with details on the ^{16}O–^{18}O isotope shifts for the three fine-structure components of this line. These lines were previously probed and calibrated in the VUV study by Herzberg (1958).

At shorter wavelengths, autoionizing states are observed displaying significant broadening as shown in Figure 8. In Figure 9, the spectrum of a rather strong resonance to the $3d''$ ^3P_J level, observed at 726 Å, is displayed. The spectrum covers transitions from all three levels in the $2p^4$ ^3P_J ground-state triplet and shows the much smaller and barely resolved splittings in the excited ^3P_J triplet. In Figure 10 a spectrum is shown of $2s^2 2p^4$–$2s 2p^5$ core excitation transitions for both ^{16}O and ^{18}O. These transitions exhibit the largest isotope shifts.

The ultraviolet spectrum of O I predominantly covers excitation from the $2p^4$ ^3P ground state to excited states of $2p^3 ns$ or np configurations, where ^3L terms yield the largest intensity. In addition, absorptions from the $^1D_2$ metastable level at 15,867.862 cm^{-1}, associated with the same $2p^4$ configuration, were also observed. No transitions from the $^1S_0$ metastable level at 33,792.583 cm^{-1} above the $^3P_2$ ground level were observed.

For states converging to the O II (^2D_J) limit, the assignments of ns' ^3D_J and nd' ^3P_J series are straightforward as the fine-structure splitting of the ground state is well resolved.
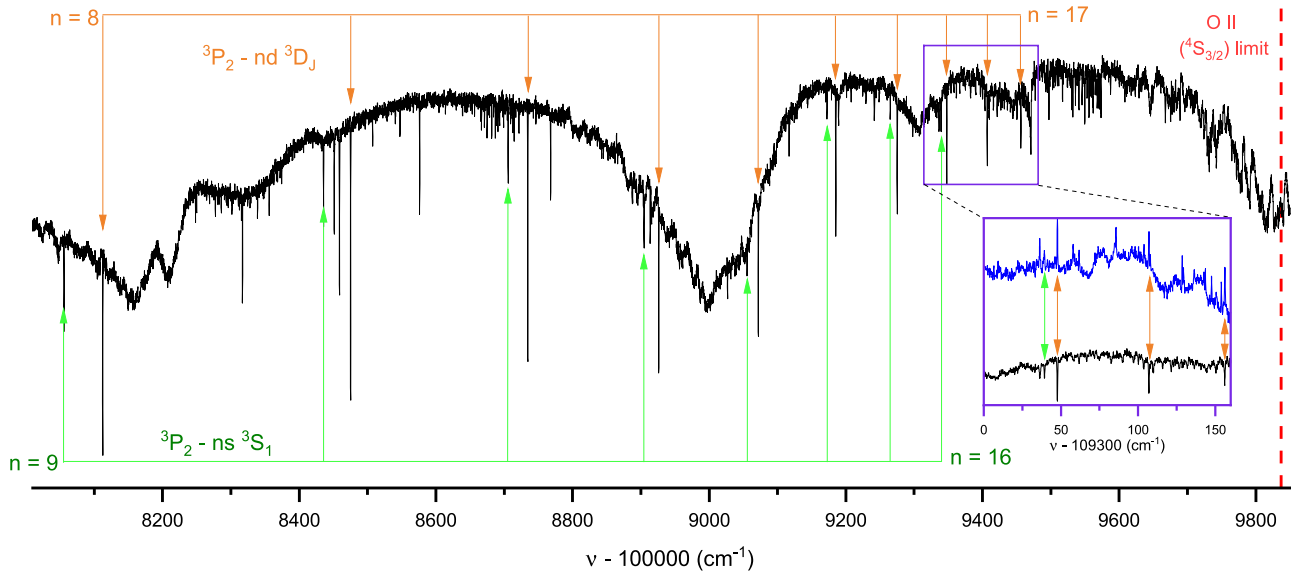
Figure 5. Example VUV FT spectrum of sharp atomic oxygen lines with assignments as indicated. O I progressions from the $^3P_2$ ground state are indicated. The progression of ns and nd Rydberg series, excited from the ground state and converging to the $^4S_{3/2}$ in the O II ion are followed to $n = 16$ and $n = 17$, respectively. The inset shows spectra of ^{16}O (in black) and ^{18}O (in blue) in the region involving $16s$ $^3S_1$ and nd $^3D_3$ from $n = 15$ to 17. The broad and strong absorption bands are from molecular oxygen ($^{16}O_2$) that was used as precursor gas. Also some molecular bands features consisting of narrow lines pertaining to N_2 and CO are observed.

However, most of members in ghd nd' $^3S_1$ and nd' ^3D_J series are observed only in excitation from the $^3P_2$ ground level. Figure 6 shows that the nd' $^3S_1$ and nd' $^3D_3$ series form a pair of doublets for $n = 12 - 16$. The stronger resonance in the doublet is assigned with $^3P_2$–nd' $^3S_1$ based on its relative strength. It is noteworthy that the separation of the doublet increases with n, where nd' $^3D_3$ has higher energy. This indicates the change in order of the level energy between nd' $^3D_3$ and nd' $^3S_1$ for higher n. The spin-forbidden transitions from the ground state to nd' $^1P_1$ and $^1D_2$ are also observed in the same range for the first time.

The states above the O II ($^4S_{3/2}$) limit, such as the ns' ^3D_J, nd' $^3S_1$ and nd' ^3D_J series, autoionize into the O I continuum under the LS-coupling approximation. Most of the observed resonances have a FWHM around 0.5 cm^{-1}. In the ns' ^3D_J series, the $^3P_2$–$4s'$ $^3D_3$ line appears as a broad resonance with 5.3(3) cm^{-1} FWHM, as was also found in Dehmer et al. (1977). From that study, the natural line widths for the $3d'$ $^3S_1$ and $3d'$ ^3D_J states are estimated to be similar as for $4s'$ $^3D_3$. However, transitions involving these states are not observed in the present study. The $^3P_2$–$4d'$ $^3S_1$ and $^3P_2$–$4d'$ $^3D_3$ lines are observed with a slightly broadened profile of 1.9(1) and 3.5(2) cm^{-1} FWHM, respectively. In contrast, no significant broadening is observed for the nd' ^3P_J series for $3 \leqslant n \leqslant 11$.

For states converging to the O II (^2P) limit, only the $3s''$ ^3P_J and nd'' ^3P_J series are observed. The $4s''$ ^3P_J states are expected to lie below the O II(^2D) limit and hence their autoionization rates are not larger than that of $3s''$ ^3P_J. However, no unassigned sharp resonance is found around 136,000 cm^{-1}. For nd'' ^3P_J and ^3D_J, these levels fall above the O II(^2D) limit and are subject to autoionization. Nevertheless their line width remains narrow. We have observed resonances from $n = 3 - 14$ with few fine-structure components resolved. For $n = 3$, the multiplet observed in Figure 9 is assigned to be ^3P_J–$3d''$ ^3P_J instead of the assignment as ^3P_J–$3d''$ ^3D_J given by Huffman et al. (1967a). The $^3P_1$–$3d''$ $^3P_1$ transition is blended with $^3P_1$–$3d''$ $^3P_0$ to yield an asymmetric line profile. For $n \geqslant 4$, the signal-to-noise ratio is less than 2 for resonances excited from the $^3P_1$ state and toward high n. We observe that transitions from the $^3P_2$ ground state are broadened due to unresolved fine-structure components. This also hinders the determination of the upper-state assignments. With this limited information, we tentatively assign the resonance progression observed from 143,000 to 149,800 cm^{-1} as belonging to the same nd'' ^3P_J series.

3.2. Line Lists

The transition frequencies of a total of 208 lines are listed in a number of tables, grouped into several series that converge to the $^4S_{3/2}$, $^3D_{5/2,3/2}$ and ^2P ionization limits of O II. Most of the resonances in the present work have been observed and documented in the NIST database (Kramida et al. 2020) and in Huffman et al. (1967a, 1967b). The fine-structure components of some transitions can be resolved thanks to the enhanced resolution of the present experiment. The assignment of newly resolved resonances are aided by taking combination differences of the precisely known fine-structure splittings in the ground ^3P_J triplet and from expected line strengths.

Tables 1 and 2 cover the transitions to the ns $^3S_1$ and nd ^3D_J Rydberg series converging to the O II ($^4S_{3/2}$) limit. These ns and nd series have been observed with n up to 16 and 17, respectively. The fine-structure splitting of the nd ^3D_J levels cannot be resolved, as it is less than 0.1 cm^{-1} for $n > 4$. These splittings were previously measured via laser spectroscopy (Ivanov et al. 2008). The next tables present line lists of the different Rydberg series converging to the O II (^2D) limit: Table 3 for the ns' ^3D_J series, Table 4 for the nd' $^3S_1$ series, Table 5 for the nd' ^3P_J series, and Table 6 for the nd' ^3D_J series. This is followed by tables presenting Rydberg series converging to the O II (^2P) limit: Table 7 for the ns'' ^3P series, and Table 8 for the nd'' ^3P series. In Table 9 some additional transitions in O I are collected: first, spin-changing transitions from the $^3P_2$ ground level to a number of singlet states ($^1P_1$ and $^1D_2$), second, transitions from the metastable $^1D_2$ level to higher-lying singlet states, and third, some inner-core excitations from $2s^22p^4$ to the $2s2p^5$ configuration.
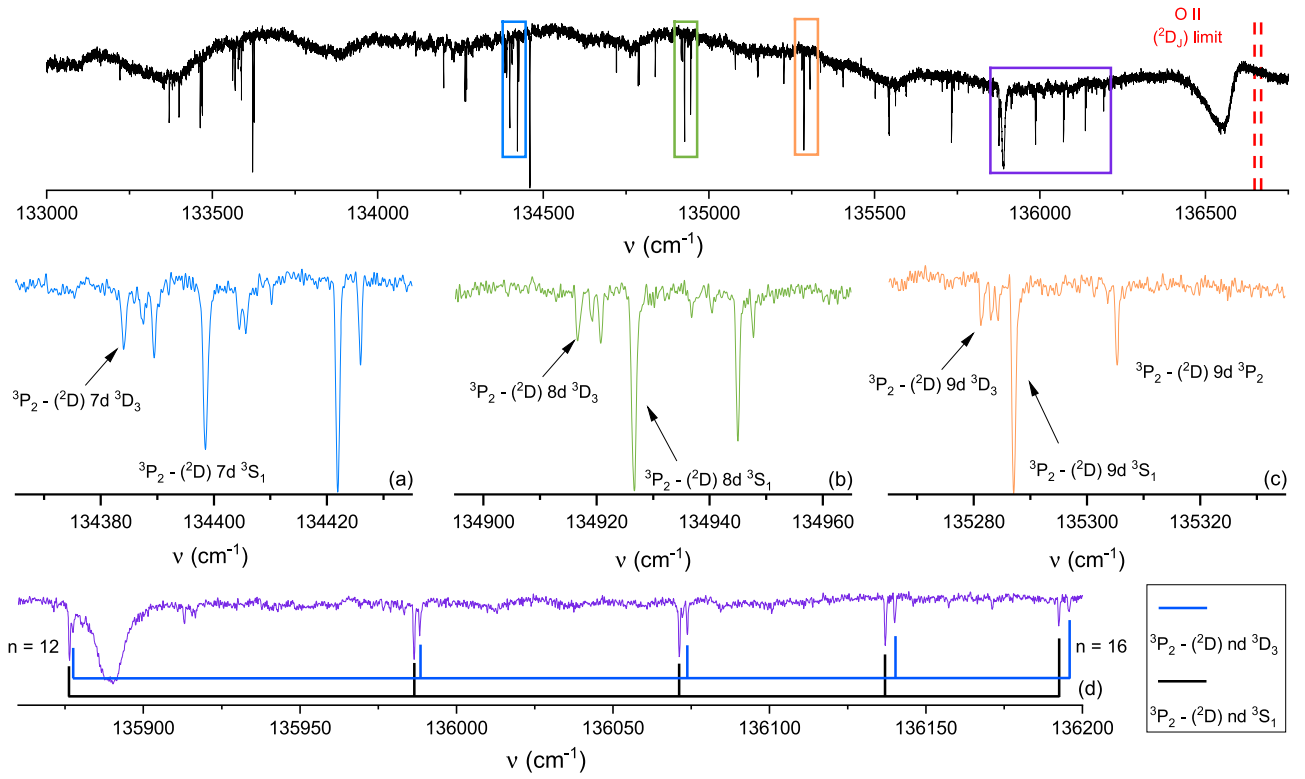
Figure 6. Overview VUV FT spectrum in the range 133,000–136,600 cm^{-1} mainly covering the O I ns' and nd' Rydberg series converging to the ^{2}D state in the O II. Certain (boxed) parts of the spectrum are enlarged in the subpanels displayed below with assignments indicated. Trace (a) to (d) shows the change of order in nd' ^{3}D$_J$ and nd' ^{3}S$_1$ level energy. Two strong principal resonance lines of Ne I (Eikema et al. 1994) are markedly present in this range.
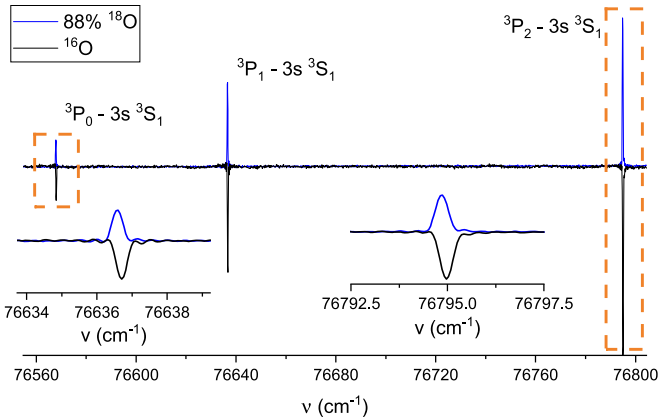

Figure 7. Spectra of the strong principal resonance line in O I $(2p^4\ ^3P_J - 2p^3 3s\ ^3S_1)$ at 1302 Å showing the fine-structure triplet of the ground ^{3}P state. The upper trace is for the ^{18}O isotope while the lower trace is the main ^{16}O isotope, with the insets showing a detailed view of the strongest and weakest components.
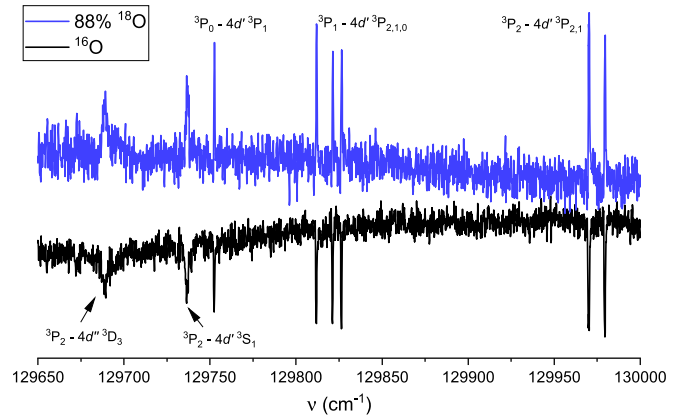

Figure 8. Autoionization effect seen in the spectra probing $4d'\ ^3L_J$ components in O I in excitation from the ground state. Significant broadening for transitions to $4d'\ ^3S_1$ and $4d'\ ^3D_3$ is observed, in contrast to sharp transitions to $4d'\ ^3P_J$, for which autoionization is forbidden under the LS-coupling approximation.

3.3. Extracted Level Energies

A global reanalysis of level energies of O I is performed that includes the 208 accurate transition frequencies measured in the present experiment and listed in the tables. This set of data is augmented with the relevant data from literature to obtain a database of level energies of higher accuracy than is currently available as the often used NIST database (Kramida et al. 2020). The ground-state fine-structure splittings, measured with extreme accuracy via far-infrared studies, are included (Zink et al. 1991; De Natale et al. 1993). In addition two accurate dipole-forbidden transitions, $2p^4\ ^3P_2 - 2p^4\ ^1D_2$ and $2p^4\ ^3P_1 - 2p^4\ ^1D_2$, from Eriksson (1965) are used to connect the ^{1}D$_2$

metastable level within the ground electronic configuration. The accurate transition energies obtained by XUV-laser spectroscopy of Ivanov et al. (2008), more accurate than the present comprehensive set, are included as well. The treatment of the upper-state fine-structure splittings in the $nd\ ^3$D$_{3,2,1}$ state requires separate mention. In the present study those small splittings are not resolved for any n value. Not even effects of the line width broadening or asymmetry are observed when probing these states. In contrast these splittings are well resolved in the laser spectroscopic studies of Ivanov et al. (2008) for $n = 3$ and 4 levels, but for $n = 5$ these splittings were not resolved. In the present study the excited $nd\ ^3$D$_{3,2,1}$ levels were probed from various well-resolved ground-state levels.
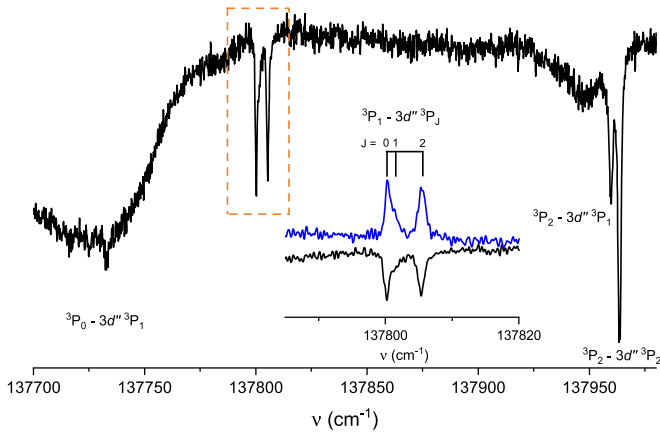
Figure 9. Spectrum of the strong resonance line in O I ($2p^4\ ^3P_J$–$3d''\ ^3P_J$) at 726 Å showing the fine-structure triplet of the ground ^3P state. The inset shows a detailed view of the $^3P_1$–$3d''\ ^3P_J$ components for both ^{16}O (in black) and ^{18}O (in blue) isotopes.
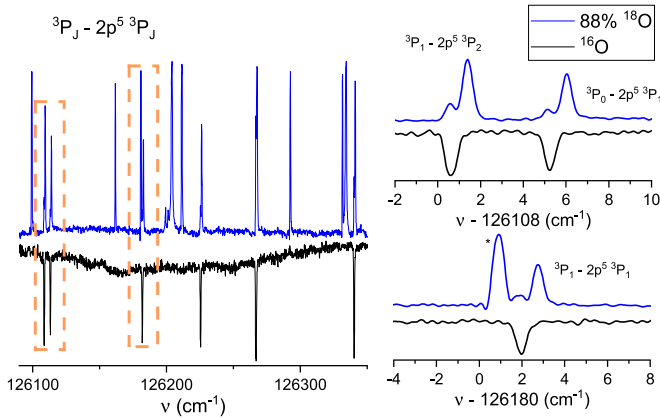

Figure 10. Spectra of some core-changing lines in O I ($2s^2 2p^4\ ^3P_J$–$2s2p^5\ ^3P_J$) at 793 Å. The right panel shows the enlarged spectra of $^3P_1$–$2s2p^5\ ^3P_2$, $^3P_0$–$2s2p^5\ ^3P_1$ and $^3P_1$–$2s2p^5\ ^3P_1$ transition for ^{18}O and ^{16}O. The ^{18}O spectra (in blue) shows a doublet for each transition, where the weaker peaks are identified as residual ^{16}O resonance. In the ^{18}O spectrum some particularly strong ns and nd Rydberg series of Ar I appear originating from the noble gas admixture in the DC discharge; note that Ar has its ionization limit at 127,109.842 cm^{-1}.

Their relative level ordering and level energy could be derived in a global fitting procedure when including the many observed lines, using the LOPT code package (Kramida 2011). We decided to include deduced values for the $^3D_{3,2,1}$ levels, even when the relative splittings were smaller than the calibration uncertainty. The result of a least-squares optimization for extracting the level energies of O I through the LOPT program (Kramida 2011) is tabulated in Table 11. The presented level energies and uncertainties are relative to the lowest-lying $2p^4\ ^3P_2$ state. Note that this level list pertains only to the main ^{16}O isotope of oxygen.

In Table 11 a comparison is made with the NIST database of level energies. The NIST compilation is based on the work by Eriksson and Isberg carried out in the 1960s via spectroscopy in the visible domain (Eriksson & Isberg 1963, 1964; Eriksson 1965; Eriksson & Isberg 1968; Isberg 1968) and probing the low-n states and on the VUV absorption measurements by Huffman et al. (1967a, 1967b) that extends to higher n values. The accuracy of these high-n levels is limited to ±2 cm^{-1}. A comprehensive comparison between level energies from the present LOPT analysis and the NIST database is graphically

Table 1
Transition Frequencies of O I Lines for Both ^{16}O and ^{18}O in Excitation from the $2s^2 2p^4\ ^3P_J$ Electronic Ground Configuration for the $ns\ ^3S_1$ Rydberg Series Converging to the $^4S_{3/2}$ Lowest Level in O II

		(^{4}S) $ns\ ^3S_1$ Series		
		^{16}O	^{18}O	Δ_{18-16}
$^3P_0$	$3s\ ^3S_1$	76,567.992	76,567.864	−0.128
$^3P_1$	$3s\ ^3S_1$	76,636.708	76,636.583	−0.125
$^3P_2$	$3s\ ^3S_1$	76,794.978	76,794.856	−0.122
$^3P_0$	$4s\ ^3S_1$	95,998.040		
$^3P_1$	$4s\ ^3S_1$	96,066.765	96,066.763	−0.001
$^3P_2$	$4s\ ^3S_1$	96,225.055	96,225.029	−0.026
$^3P_0$	$5s\ ^3S_1$	102,184.958		
$^3P_1$	$5s\ ^3S_1$	102,253.701		
$^3P_2$	$5s\ ^3S_1$	102,411.974		
$^3P_0$	$6s\ ^3S_1$	104,938.208		
$^3P_1$	$6s\ ^3S_1$	105,006.936	105,006.981	0.045
$^3P_2$	$6s\ ^3S_1$	105,165.207	105,165.191	−0.016
$^3P_2$	$7s\ ^3S_1$	106,627.926	106,627.967	0.041
$^3P_2$	$8s\ ^3S_1$	107,497.204	107,497.243	0.040
$^3P_1$	$8s\ ^3S_1$	107,338.927	107,338.987	0.060
$^3P_2$	$9s\ ^3S_1$	108,055.637	108,055.697	0.060
$^3P_2$	$10s\ ^3S_1$	108,435.611		
$^3P_2$	$11s\ ^3S_1$	108,705.792		
$^3P_2$	$12s\ ^3S_1$	108,904.695	108,904.738	0.044
$^3P_2$	$13s\ ^3S_1$	109,055.364	109,055.471	0.107
$^3P_2$	$14s\ ^3S_1$	109,172.358	109,172.411	0.053
$^3P_2$	$15s\ ^3S_1$	109,264.869	109,264.974	0.105
$^3P_2$	$16s\ ^3S_1$	109,339.285	109,339.316	0.031

Note. Values in units of cm^{-1}. The uncertainty for each transition frequency in column 3 and that of the ^{18}O–^{16}O isotope shift, Δ_{18-16}, in column 4 are 0.035 cm^{-1} and 0.050 cm^{-1}, respectively.

displayed in Figure 11. These comparisons, both in Table 11 and in Figure 11, show that for the levels obtained from the work by Eriksson and coworkers, i.e., the extracted level energies for $n \leqslant 8$ of (^{4}S) $ns\ ^3S_1$, $n \leqslant 7$ of (^{4}S) $nd\ ^3D_J$, some of low-n (^{2}D) and (^{2}P) states show good agreement. The averaged difference between the data sets is -0.006 cm^{-1} and the rms deviation is as low as 0.022 cm^{-1} for excitation levels below 108,000 cm^{-1}. So for these levels consistency is found within the uncertainty of the present experiment. As a specific example, the most accurate excitation energy of the $3s\ ^3S_1$ level before this study was determined by Herzberg (1958) some 60 years ago. The present study verifies and improves this accuracy, if only by a small margin.

The higher-lying level energies in the NIST database, as taken from Huffman's measurements, show a significant discrepancy with the present data set. For levels lying energetically above 108,000 cm^{-1}, and converging to the (^{4}S) O II limit, an average difference -1.35 cm^{-1} with a 1.53 cm^{-1} rms deviation is found, indicating a systematic shift in Huffman's measurements in this range. For levels above the (^{4}S) O II first ionization limit, the distribution yields an averaged difference of 0.69 cm^{-1} and an rms deviation 3.43 cm^{-1}. Some of the larger discrepancies are associated with misassignments. We have revised some of the assignments made in Huffman et al. (1967a) for (^{2}D) and (^{2}P) nl series. For example, Huffman had labeled the transitions from the $^3P_2$ ground level to the $8d$ – $10d\ ^3S_1$ levels as one of the triplets shown in Figure 6. The transitions to $n > 7$ levels for the triplet S and D series are of relevance for the assignment of high-redshift astronomical spectra, for which examples are

Table 2
Transition Frequencies of O I Lines for both ^{16}O and ^{18}O in Excitation from the $2s^2 2p^4$ ^3P_J Electronic Ground Configuration to the nd ^3D_J Rydberg Series Converging to the $^4S_{3/2}$ Lowest Level in O II

		(^{4}S) nd ^3D_J Series		
		^{16}O	^{18}O	Δ_{18-16}
$^3P_0$	$3d$ $^3D_1$	97,261.367	97,261.379	0.012
$^3P_1$	$3d$ $^3D_2$	97,330.172	97,330.145	−0.027
$^3P_2$	$3d$ $^3D_3$	97,488.542	97,488.527	−0.015
$^3P_0$	$4d$ $^3D_1$	102,681.496		
$^3P_1$	$4d$ $^3D_2$	102,750.163		
$^3P_2$	$4d$ $^3D_3$	102,908.380		
$^3P_0$	$5d$ $^3D_1$	105,182.019		
$^3P_1$	$5d$ $^3D_2$	105,250.740	105,250.746	0.006
$^3P_2$	$5d$ $^3D_3$	105,409.005	105,409.051	0.046
$^3P_1$	$6d$ $^3D_2$	106,607.531	106,607.560	0.029
$^3P_2$	$6d$ $^3D_3$	106,765.804	106,765.845	0.040
$^3P_0$	$7d$ $^3D_1$	107,355.757	107,355.798	0.041
$^3P_1$	$7d$ $^3D_2$	107,424.486	107,424.542	0.055
$^3P_2$	$7d$ $^3D_3$	107,582.778	107,582.830	0.052
$^3P_1$	$8d$ $^3D_2$	107,954.116	107,954.177	0.061
$^3P_2$	$8d$ $^3D_3$	108,112.415	108,112.451	0.036
$^3P_0$	$8d$ $^3D_1$	107,885.387	107,885.455	0.068
$^3P_1$	$9d$ $^3D_2$	108,316.912	108,316.902	−0.009
$^3P_2$	$9d$ $^3D_3$	108,475.182	108,475.229	0.047
$^3P_0$	$10d$ $^3D_1$	108,507.431		
$^3P_1$	$10d$ $^3D_2$	108,576.192	108,576.237	0.046
$^3P_2$	$10d$ $^3D_3$	108,734.455	108,734.508	0.053
$^3P_1$	$11d$ $^3D_2$	108,767.919	108,767.952	0.033
$^3P_2$	$11d$ $^3D_3$	108,926.160	108,926.213	0.053
$^3P_1$	$12d$ $^3D_2$	108,913.626	108,913.664	0.038
$^3P_2$	$12d$ $^3D_3$	109,071.897	109,071.952	0.055
$^3P_1$	$13d$ $^3D_2$	109,026.974	109,027.072	0.098
$^3P_2$	$13d$ $^3D_3$	109,185.275	109,185.313	0.038
$^3P_2$	$14d$ $^3D_3$	109,275.149	109,275.203	0.054
$^3P_1$	$15d$ $^3D_2$	109,189.422	109,189.425	0.004
$^3P_2$	$15d$ $^3D_3$	109,347.675	109,347.713	0.039
$^3P_2$	$16d$ $^3D_3$	109,407.001	109,407.054	0.054
$^3P_2$	$17d$ $^3D_3$	109,456.187	109,456.247	0.060

Note. Values in units of cm^{-1}. The uncertainty for each transition frequency in column 3 and that of the ^{18}O–^{16}O isotope shift, Δ_{18-16}, in column 4 are 0.035 cm^{-1} and 0.050 cm^{-1}, respectively.

Table 3
Transition Frequencies of O I Lines for ^{16}O and ^{18}O in Excitation from the $2s^2 2p^4$ Configuration to Rydberg Series Converging to the ^2D Limit in O II: the ns' ^3D_J Series

		(^{2}D) ns' ^3D_J Series		
		^{16}O	^{18}O	Δ_{18-16}
$^3P_0$	$3s'$ $^3D_1$	100,928.425	100,928.361	−0.064
$^3P_1$	$3s'$ $^3D_1$	100,997.139	100,997.116	−0.023
$^3P_2$	$3s'$ $^3D_1$	101,155.414		
$^3P_1$	$3s'$ $^3D_2$	100,989.244	100,989.226	−0.018
$^3P_2$	$3s'$ $^3D_2$	101,147.513	101,147.495	−0.049
$^3P_2$	$3s'$ $^3D_3$	101,135.390	101,135.341	−0.167
$^3P_2$	$4s'$ $^3D_3$	122,420.0(5)	122,420.9(5)	0.9(7)
$^3P_2$	$5s'$ $^3D_3$	128,979.212	128,979.045	−0.167
$^3P_1$	$6s'$ $^3D_2$	131,707.405	131,707.722	0.317
$^3P_2$	$6s'$ $^3D_3$	131,855.294	131,855.405	0.111
$^3P_2$	$6s'$ $^3D_2$	131,865.843		
$^3P_1$	$7s'$ $^3D_2$	133,221.441	133,221.544	0.102
$^3P_2$	$7s'$ $^3D_3$	133,370.215	133,370.292	0.077
$^3P_2$	$7s'$ $^3D_2$	133,379.7(1)	133,379.9(1)	0.2(1)
$^3P_1$	$8s'$ $^3D_2$	134,115.292	134,115.446	0.154
$^3P_2$	$8s'$ $^3D_3$	134,265.424	134,265.501	0.077
$^3P_2$	$9s'$ $^3D_3$	134,838.192	134,838.275	0.084
$^3P_2$	$10s'$ $^3D_3$	135,226.729	135,226.799	0.069
$^3P_2$	$11s'$ $^3D_3$	135,502.317	135,502.358	0.041
$^3P_2$	$12s'$ $^3D_3$	135,704.808	135,704.874	0.065

Note. Values in units of cm^{-1}. Unless specified, the uncertainty for each transition frequency in column 3 and that of the ^{18}O–^{16}O isotope shift, Δ_{18-16}, in column 4 are 0.035 cm^{-1} and 0.050 cm^{-1}, respectively.

Table 4
Transition Frequencies of O I Lines for ^{16}O and ^{18}O in Excitation from the $2s^2 2p^4$ Configuration to Rydberg Series Converging to the ^2D Limit in O II: the nd' $^3S_1$

		(^{2}D) nd' $^3S_1$ Series		
		^{16}O	^{18}O	Δ_{18-16}
$^3P_2$	$4d'$ $^3S_1$	129,736.6(2)	129,736.7(2)	0.1(3)
$^3P_1$	$5d'$ $^3S_1$	132,075.2(1)	132,075.4(1)	0.2(1)
$^3P_2$	$5d'$ $^3S_1$	132,233.551	132,233.686	0.134
$^3P_2$	$6d'$ $^3S_1$	133,578.530	133,578.606	0.076
$^3P_2$	$7d'$ $^3S_1$	134,398.555	134,398.664	0.109
$^3P_2$	$8d'$ $^3S_1$	134,926.643	134,926.720	0.077
$^3P_2$	$9d'$ $^3S_1$	135,287.096	135,287.176	0.080
$^3P_2$	$10d'$ $^3S_1$	135,544.556	135,544.682	0.127
$^3P_2$	$11d'$ $^3S_1$	135,733.090	135,733.179	0.089
$^3P_2$	$12d'$ $^3S_1$	135,876.417	135,876.523	0.106
$^3P_2$	$13d'$ $^3S_1$	135,986.501	135,986.613	0.112
$^3P_2$	$14d'$ $^3S_1$	136,071.238	136,071.309	0.071
$^3P_2$	$15d'$ $^3S_1$	136,137.057	136,137.156	0.099
$^3P_2$	$16d'$ $^3S_1$	136,192.498	136,192.654	0.156

Note. Values in units of cm^{-1}. Unless specified, the uncertainty for each transition frequency in column 3 and that of the ^{18}O–^{16}O isotope shift, Δ_{18-16}, in column 4 are 0.035 cm^{-1} and 0.050 cm^{-1}, respectively.

given in Section 4. The values for these levels are largely improved in the present study, taking advantage of the accuracy that is a factor of 50 times better than in the 1960s (Huffman et al. 1967a, 1967b).

A second comparison can be made between this study and the level energy database associated with the comprehensive study by Civiš et al. (2018), which is not yet included in the NIST database. Those measurements were carried out in the near-infrared region (800–13,000 cm^{-1}), mostly probing levels of high angular momentum. The accurate data from Ivanov et al. (2008) and Marinov et al. (2017) were included in their level analysis, in addition to the earlier accurate data by Eriksson and coworkers (Eriksson & Isberg 1963, 1964; Eriksson 1965; Eriksson & Isberg 1968; Isberg 1968). Civiš et al. performed a comprehensive reevaluation of O I level energies with $2p^3(^4S)nl$ configuration with n up to 8. The high-precision XUV-laser spectroscopic data from Ivanov et al. (2008) are in fact used as anchors for the IR lines in their level analysis. Not considering the literature data mentioned, there are only six independent levels to be compared between the present data set and that of Civiš et al. A comparison shows that these six levels

are in perfect agreement, within 0.010 cm^{-1}, well within the uncertainty margin of the present experiment.

3.4. Isotope Shift

The isotope shift stems from the motion of the nucleus of finite mass M within the atomic center-of-mass reference frame. The conservation of momentum $\boldsymbol{P} + \sum_i p_i = 0$, with the nuclear momentum $\boldsymbol{P}$ and individual electronic momentum p_i, leads to

Table 5
Transition Frequencies of O I Lines for ^{16}O and ^{18}O in Excitation from the $2s^22p^4$ Configuration to Rydberg Series Converging to the ^{2}D Limit in O II: the nd' ^{3}P$_J$

		(^{2}D) nd' ^{3}P$_J$ Series		
		^{16}O	^{18}O	Δ_{18-16}
^{3}P$_0$	$3d'$ ^{3}P$_1$	123,128.595	123,128.997	0.402
^{3}P$_1$	$3d'$ ^{3}P$_1$	123,197.274	123,197.704	0.430
^{3}P$_1$	$3d'$ ^{3}P$_2$	123,138.499	123,138.980	0.481
^{3}P$_2$	$3d'$ ^{3}P$_2$	123,296.793	123,297.241	0.449
^{3}P$_1$	$4d'$ ^{3}P$_0$	129,826.320	129,826.386	0.066
^{3}P$_0$	$4d'$ ^{3}P$_1$	129,752.426	129,752.519	0.093
^{3}P$_1$	$4d'$ ^{3}P$_1$	129,821.114	129,821.205	0.092
^{3}P$_2$	$4d'$ ^{3}P$_1$	129,979.401	129,979.492	0.091
^{3}P$_1$	$4d'$ ^{3}P$_2$	129,811.752	129,811.855	0.103
^{3}P$_2$	$4d'$ ^{3}P$_2$	129,970.034	129,970.132	0.098
^{3}P$_1$	$5d'$ ^{3}P$_0$	132,160.389	132,160.482	0.094
^{3}P$_0$	$5d'$ ^{3}P$_1$	132,089.150	132,089.223	0.073
^{3}P$_1$	$5d'$ ^{3}P$_1$	132,157.854	132,157.956	0.102
^{3}P$_2$	$5d'$ ^{3}P$_1$	132,316.116	132,316.221	0.104
^{3}P$_1$	$5d'$ ^{3}P$_2$	132,152.238	132,152.361	0.123
^{3}P$_2$	$5d'$ ^{3}P$_2$	132,310.532	132,310.619	0.087
^{3}P$_1$	$6d'$ ^{3}P$_0$	133,470.233	133,470.263	0.030
^{3}P$_0$	$6d'$ ^{3}P$_1$	133,399.921	133,399.990	0.069
^{3}P$_1$	$6d'$ ^{3}P$_1$	133,468.601	133,468.675	0.074
^{3}P$_2$	$6d'$ ^{3}P$_1$	133,626.868	133,626.973	0.105
^{3}P$_1$	$6d'$ ^{3}P$_2$	133,463.868	133,463.921	0.054
^{3}P$_2$	$6d'$ ^{3}P$_2$	133,622.094	133,622.191	0.097
^{3}P$_1$	$7d'$ ^{3}P$_0$	134,268.279	134,268.335	0.056
^{3}P$_0$	$7d'$ ^{3}P$_1$	134,198.966	134,199.050	0.084
^{3}P$_1$	$7d'$ ^{3}P$_1$	134,267.563	134,267.651	0.088
^{3}P$_2$	$7d'$ ^{3}P$_1$	134,425.920	134,426.016	0.096
^{3}P$_1$	$7d'$ ^{3}P$_2$	134,263.668	134,263.770	0.102
^{3}P$_2$	$7d'$ ^{3}P$_2$	134,421.932	134,422.029	0.098
^{3}P$_0$	$8d'$ ^{3}P$_1$	134,720.747	134,720.811	0.064
^{3}P$_1$	$8d'$ ^{3}P$_1$	134,789.284	134,789.402	0.119
^{3}P$_2$	$8d'$ ^{3}P$_1$	134,947.721	134,947.762	0.040
^{3}P$_1$	$8d'$ ^{3}P$_2$	134,786.731	134,786.841	0.110
^{3}P$_2$	$8d'$ ^{3}P$_2$	134,944.992	134,945.092	0.100
^{3}P$_0$	$9d'$ ^{3}P$_1$	135,079.814	135,079.874	0.060
^{3}P$_1$	$9d'$ ^{3}P$_1$	135,148.484	135148.530	0.046
^{3}P$_1$	$9d'$ ^{3}P$_2$	135,147.251	135,147.373	0.123
^{3}P$_2$	$9d'$ ^{3}P$_2$	135,305.312	135,305.393	0.081
^{3}P$_0$	$10d'$ ^{3}P$_1$	135,337.015	135,337.033	0.018
^{3}P$_1$	$10d'$ ^{3}P$_1$	135,405.295	135,405.489	0.193
^{3}P$_2$	$10d'$ ^{3}P$_2$	135,563.574	135,563.639	0.065
^{3}P$_1$	$11d'$ ^{3}P$_1$	135,595.6(3)	135,596.3(3)	0.7(4)
^{3}P$_2$	$11d'$ ^{3}P$_2$	135,754.533	135,754.693	0.160

Note. Values in units of cm^{-1}. Unless specified, the uncertainty for each transition frequency in column 3 and that of the ^{18}O–^{16}O isotope shift, Δ_{18-16}, in column 4 are 0.035 cm^{-1} and 0.050 cm^{-1}, respectively.

Table 6
Transition Frequencies of O I Lines for ^{16}O and ^{18}O in Excitation from the $2s^22p^4$ Configuration to nd' ^{3}D$_J$ Rydberg Series Converging to the ^{2}D Limit in O II

		(^{2}D) nd' ^{3}D$_J$ Series		
		^{16}O	^{18}O	Δ_{18-16}
^{3}P$_2$	$4d'$ ^{3}D$_3$	129,689.7(4)	129,689.1(4)	−0.6(6)
^{3}P$_2$	$5d'$ ^{3}D$_3$	132,194.973	132,195.079	0.106
^{3}P$_2$	$6d'$ ^{3}D$_3$	133,561.905	133,561.977	0.072
^{3}P$_2$	$6d'$ ^{3}D$_2$	133,566.294	133,566.428	0.134
^{3}P$_2$	$7d'$ ^{3}D$_3$	134,384.100	134,384.220	0.119
^{3}P$_2$	$7d'$ ^{3}D$_2$	134,387.443	134,387.495	0.053
^{3}P$_2$	$8d'$ ^{3}D$_3$	134,916.743	134,916.859	0.116
^{3}P$_2$	$8d'$ ^{3}D$_2$	134,919.174	134,919.214	0.040
^{3}P$_2$	$9d'$ ^{3}D$_3$	135,281.413	135,281.466	0.053
^{3}P$_2$	$9d'$ ^{3}D$_2$	135,283.132	135,283.221	0.089
^{3}P$_2$	$10d'$ ^{3}D$_3$	135,542.831	135,542.915	0.084
^{3}P$_2$	$10d'$ ^{3}D$_2$	135,544.110	135,544.210	0.100
^{3}P$_2$	$11d'$ ^{3}D$_3$	135,734.868	135,734.971	0.103
^{3}P$_2$	$11d'$ ^{3}D$_2$	135,735.971		
^{3}P$_2$	$12d'$ ^{3}D$_3$	135,877.446	135,877.564	0.118
^{3}P$_2$	$13d'$ ^{3}D$_3$	135,988.295	135,988.401	0.106
^{3}P$_2$	$14d'$ ^{3}D$_3$	136,073.778	136,073.870	0.092
^{3}P$_2$	$15d'$ ^{3}D$_3$	136,140.060	136,140.184	0.124
^{3}P$_2$	$16d'$ ^{3}D$_3$	136,195.729	136,195.751	0.022

Note. Values in units of cm^{-1}. Unless specified, the uncertainty for each transition frequency in column 3 and that of the ^{18}O–^{16}O isotope shift, Δ_{18-16}, in column 4 are 0.035 cm^{-1} and 0.050 cm^{-1}, respectively.

Table 7
Transition Frequencies of O I Lines in ^{16}O and ^{18}O Originating in the $2s^22p^4$ ^{3}P$_2$ Ground Level and Exciting the Rydberg States Converging to the ^{2}P limit in O II: the ns'' ^{3}P$_J$ Series

		(^{2}P) ns'' ^{3}P$_J$ Series		
		^{16}O	^{18}O	Δ_{18-16}
^{3}P$_0$	$3s''$ ^{3}P$_1$	113,694.391	113,694.449	0.058
^{3}P$_1$	$3s''$ ^{3}P$_2$	113,752.677	113,752.725	0.047
^{3}P$_1$	$3s''$ ^{3}P$_1$	113,763.115	113,763.161	0.046
^{3}P$_1$	$3s''$ ^{3}P$_0$	113,769.251	113,769.297	0.046
^{3}P$_2$	$3s''$ ^{3}P$_2$	113,910.929	113,911.007	0.078
^{3}P$_2$	$3s''$ ^{3}P$_1$	113,921.351	113,921.435	0.084

Note. Values in units of cm^{-1}. The uncertainty for each transition frequency in column 3 and that of the ^{18}O–^{16}O isotope shift, Δ_{18-16}, in column 4 are 0.035 cm^{-1} and 0.050 cm^{-1}, respectively.

the expression of the kinetic energy operator for the nucleus

$$\frac{\boldsymbol{P}^2}{2M} = \frac{1}{2M}\sum_i \boldsymbol{p}_i^2 + \frac{1}{2M}\sum_{i\neq j}\boldsymbol{p}_i \cdot \boldsymbol{p}_j. \tag{1}$$

The expectation value of the first operator on the right-hand side is the Bohr shift or normal mass shift (NMS) that is proportional to the Rydberg constant and results in a blueshift for the heavier isotope. The second operator refers to the specific mass shift (SMS) that is related to electron correlation, so that its magnitude and sign is highly dependent on the specific electronic level involved. In the transition energy

measurements of the present study, the isotope shifts accessed comprise of contributions from both the upper and lower levels involved.

Many of the transitions listed in Tables 1–9 have been observed for both the main ^{16}O isotope, as well as from an ^{18}O-enriched sample. It is for the first time that such a comprehensive isotope shift analysis is performed in the VUV region for the oxygen atom. In general, the ^{18}O -^{16}O isotope shifts for each transition are derived with 0.05 cm^{-1} uncertainty, unless specifically indicated in between parentheses for the blended or weak lines. From among the 165 transitions with isotope shifts determined, we highlight three sets of transitions, 2p^4 ^{3}P$_J$–(^{4}S) 3s ^{3}S$_1$, 2p^4 ^{3}P$_J$–(^{2}D) 3d' ^{3}P$_J$, and 2p^4 ^{3}P$_J$–2s2p^5 ^{3}P$_J$, as representative cases.

The isotope shift for the strongest fine-structure component of the principal line 2p^4 ^{3}P$_2$–(^{4}S) 3s ^{3}S$_1$ transition is determined

Table 8
Transition Frequencies of O I Lines in ^{16}O and ^{18}O Originating in the $2s^2 2p^4$ $^3P_2$ Ground Level and Exciting the Rydberg States Converging to the ^2P Limit in O II: the nd'' ^3P_J Series

		(^2P) nd'' ^3P_J Series		
		^{16}O	^{18}O	Δ_{18-16}
$^3P_0$	$3d''$ $^3P_1$	137,732.801	137,732.969	0.168
$^3P_0$	$3d''$ $^3P_0$	137,800.165	137,800.275	0.109
$^3P_1$	$3d''$ $^3P_1$	137,801.1(2)	137,801.0(2)	−0.1(3)
$^3P_1$	$3d''$ $^3P_2$	137,805.341	137,805.488	0.147
$^3P_2$	$3d''$ $^3P_1$	137,959.786	137,959.843	0.057
$^3P_2$	$3d''$ $^3P_2$	137,963.573	137,963.730	0.157
$^3P_0$	$4d''$ $^3P_1$[a]	143,137.2(2)		
$^3P_1$	$4d''$ $^3P_2$[a]	143,207.0(2)		
$^3P_2$	$4d''$ $^3P_2$[a]	143,365.3(2)		
$^3P_2$	$5d''$ $^3P_{2,1}$[a]	145,870.0(2)		
$^3P_1$	$6d''$ $^3P_0$[a]	147,070.2(2)		
$^3P_1$	$6d''$ $^3P_2$[a]	147,072.4(2)		
$^3P_2$	$6d''$ $^3P_{2,1}$[a]	147,229.5(2)		
$^3P_1$	$7d''$ $^3P_0$[a]	147,888.9(2)		
$^3P_1$	$7d''$ $^3P_2$[a]	147,890.9(2)		
$^3P_2$	$7d''$ $^3P_{2,1}$[a]	148,048.0(2)		
$^3P_1$	$8d''$ $^3P_0$[a]	148,419.6(2)		
$^3P_1$	$8d''$ $^3P_2$[a]	148,421.8(2)		
$^3P_2$	$8d''$ $^3P_{2,1}$[a]	148,578.4(2)		
$^3P_2$	$9d''$ $^3P_2$[a]	148,941.4(2)		
$^3P_2$	$9d''$ $^3P_1$[a]	148,942.9(2)		
$^3P_2$	$10d''$ $^3P_2$[a]	149,201.3(2)		
$^3P_2$	$10d''$ $^3P_1$[a]	149,202.7(2)		
$^3P_2$	$11d''$ $^3P_{2,1}$[a]	149,393.3(2)		
$^3P_2$	$12d''$ $^3P_2$[a]	149,539.0(2)		
$^3P_2$	$12d''$ $^3P_1$[a]	149,540.7(2)		
$^3P_2$	$13d''$ $^3P_{2,1}$[a]	149,652.5(2)		
$^3P_2$	$14d''$ $^3P_{2,1}$[a]	149,742.5(2)		

Note. Values in units of cm^{-1}. Unless specified, the uncertainty for each transition frequency in column 3 and that of the ^{18}O–^{16}O isotope shift, Δ_{18-16}, in column 4 are 0.035 cm^{-1} and 0.050 cm^{-1}, respectively. The transitions to $n \geqslant 4$ are tentatively assigned.
[a] Tentative assignment.

Table 9
Transition Frequencies of Some Additional Lines in the Spectrum of O I for both ^{16}O and ^{18}O

		^{16}O	^{18}O	Δ_{18-16}
$^3P_2$	$5d'$ $^1P_1$	132,205.256	132,205.486	0.229
$^3P_2$	$6d'$ $^1P_1$	133,569.174	133,569.318	0.143
$^3P_2$	$7d'$ $^1P_1$	134,389.480	134,389.553	0.073
$^3P_2$	$8d'$ $^1P_1$	134,920.742	134,920.824	0.082
$^3P_2$	$9d'$ $^1P_1$	135,284.237	135,284.432	0.195
$^3P_2$	$10d'$ $^1P_1$	135,541.830	135,541.855	0.025
$^3P_2$	$6d'$ $^1D_2$	133,588.032	133,588.179	0.147
$^3P_2$	$7d'$ $^1D_2$	134,405.663	134,405.698	0.035
$^1D_2$	$3s'$ $^1D_2$	86,794.192		
$^1D_2$	$4s'$ $^1D_2$	106,929.766		
$^1D_2$	$5s'$ $^1D_2$	113,264.474		
$^1D_2$	$6s'$ $^1D_2$	116,067.899		
$^1D_2$	$3d'$ $^1D_2$	108,451.237	108,451.265	0.028
$^1D_2$	$5d'$ $^1D_2$	116,368.582		
$^1D_2$	$5d'$ $^1F_3$	116,363.061		
$^1D_2$	$3d'$ $^1F_3$	108,458.896	108,458.909	0.013
$^1D_2$	$3s''$ $^1P_1$	100,050.254		
$^3P_1$	$2p^5$ $^3P_2$	126,108.625	126,109.397	0.772
$^3P_0$	$2p^5$ $^3P_1$	126,113.248	126,114.041	0.793
$^3P_1$	$2p^5$ $^3P_1$	126,181.971	126,182.761	0.791
$^3P_1$	$2p^5$ $^3P_0$	126,225.507	126,226.295	0.788
$^3P_2$	$2p^5$ $^3P_2$	126,266.909	126,267.678	0.769
$^3P_2$	$2p^5$ $^3P_1$	126,340.253	126,341.027	0.774

Note. This table contains (i) spin-changing transitions from the $^3P_2$ ground state into singlet excited states; (ii) transitions from the metastable $^1D_2$ level; (iii) core excitations into the $2s2p^5$ configuration. Values in units of cm^{-1}. The uncertainty for each transition frequency in column 3 and that of the ^{18}O–^{16}O the isotope shift, Δ_{18-16}, in column 4 are 0.035 cm^{-1} and 0.050 cm^{-1}, respectively.
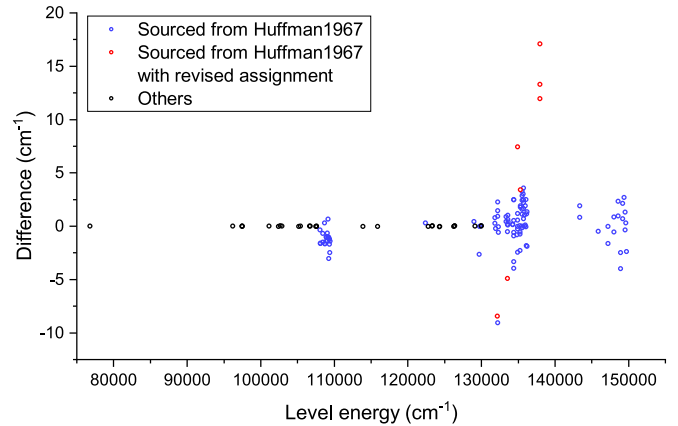

Figure 11. Comparison of the extracted level energies between the present study and values from the NIST database. The NIST level energies, sourced from the comprehensive measurements of Huffman et al. (1967a, 1967b), show significant discrepancies plotted in blue and misassignments plotted in red.

to be around $-0.122(40)$ cm^{-1} in this study (see Table 2). For this transition, the Bohr or NMS shift obtained from the measured transition energy is 0.2904 cm^{-1}; hence the SMS shift is derived to be $-0.413(40)$ cm^{-1}. The opposing signs of the NMS and SMS shifts lead to a cancellation and a smaller total isotope shift. The experimentally obtained SMS value can be compared to results of the theoretical study of Jönsson & Godefroid (2000; without fine structure). Using a Hartree–Fock (HF) model they quote an SMS shift of -0.549 cm^{-1}, while for their multiconfiguration HF and configuration interaction (CI) method they obtain an SMS shift of -0.424 cm^{-1}. The latter CI calculation result is in agreement with the present measurements, while the HF result is not.

Another interesting transition is the $2p^4$ ^3P_J–$2s2p^5$ ^3P_J line, which involves an upper state with a $2s2p^5$ configuration where one of the inner $2s$ electrons is promoted to $2p$. For these transitions, the isotope shifts observed are around 0.78 cm^{-1} (see Table 9). With the NMS shift of 0.477 cm^{-1}, the experimentally derived SMS shift is about $+0.31(5)$ cm^{-1}. In this case, the NMS and SMS shifts have the same sign and combine to a large total transition isotope shift.

As a last example, we turn to the $2p^4$ ^3P_J–(^2D) $3d'$ ^3P_J transitions with the excited state belonging to the series that converge to the second ionization limit of O II. The largest observed isotope shift is 0.48(5) cm^{-1} for this multiplet, as seen in Table 5. With an NMS shift of 0.466 cm^{-1}, the measurement yields an SMS shift of 0.01(5) cm^{-1}. The small transition SMS shift suggests a cancellation of the upper and lower level SMS shifts, and provides a benchmark to various calculation methods with its sensitivity to such cancellation effects.
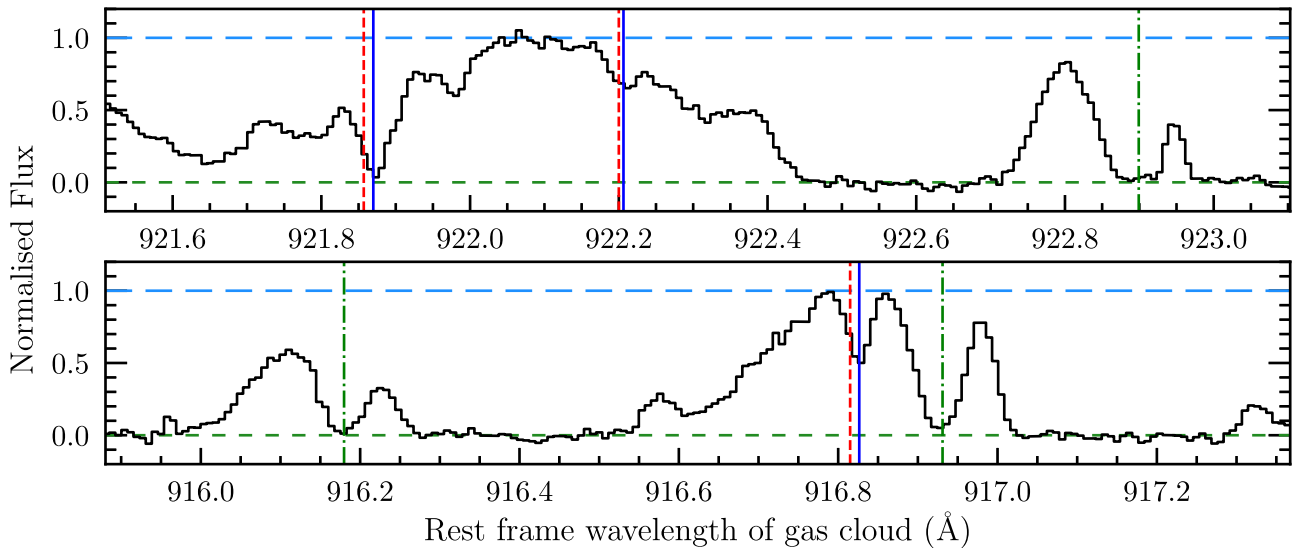
Figure 12. Astronomical spectra of a gas cloud at redshift $z = 3.70747$ toward the quasar J0814+5029 (black histogram), showing D I absorption lines (vertical green lines) and O I absorption lines. The previous laboratory wavelengths of the O I absorption lines are shown by the vertical red (dashed) lines (Moore 1993), while our VUV-FTS measurements are shown as vertical blue (solid) lines.

Comparisons of SMS shifts obtained from experiment and calculations allow for the systematic investigation of electron correlation effects, which remain challenging to calculate. The accuracy of various theoretical methods may then be assessed with the comprehensive list of ^{16}O-^{18}O isotope shifts in the present study that cover many different transitions. Furthermore, combining transition isotope shifts originating from a common lower level enable the derivation of *level* isotope shifts that may be valuable in testing the absolute accuracy of different calculation approaches.

4. Application to Astronomical Spectra

Reliable laboratory measurements of atomic transition wavelengths provide an important reference to compare with astrophysical observations. In particular, high-redshift ($z \simeq 3$) astrophysical observations provide a snapshot of the physics of the universe when it was only two to three billion years old. If the physics that governs the universe changes with time, one might expect to see departures from the wavelengths measured at two different epochs. Thus, by constructing a reliable determination of the relative offset between high-redshift astrophysical clouds and the wavelengths measured in the laboratory, we can place a limit on possible departures from the Standard Model of physics. Such a study was performed in the early days of cosmological spectroscopy by probing fine-structure splittings of oxygen ions (Bahcall & Schmidt 1967); subsequent attempts to uncover possible variations of the fine-structure constant with the redshift have yielded increasingly tighter upper limits (Kotuš et al. 2017).

As part of an investigation to uncover quiescent gas clouds at high redshift (Cooke et al. 2014), two quasars were identified (J0814+5029, R.A. = 08:14:35.18, decl. = +50:29:46; J1358 +6522, R.A. = 13:58:42.92, decl. = +65:22:36) that exhibit intrinsically narrow absorption lines of O I and deuterium D I (see Figure 12). Some O I lines exciting higher-n Rydberg states in these two cases appeared to be shifted from the D I lines when comparing to the prevailing NIST VUV databases for O I. As the rest wavelengths for D I are known to high

Table 10
Comparison of Astronomical Observations of ^{16}O Lines in Two Quasar Absorption Systems (Uncertainties within Parentheses) both with the NIST Database (Kramida et al. 2020) and the Present Study

Assignment	λ_{astro}	Δ_{NIST}	$\Delta_{present}$
	J0814 + 5029		
$2p^3 12d\ ^3D_3$	916.8266(12)	−0.0118	−0.0001
$2p^3 9d\ ^3D_3$	921.8698(35)	−0.0129	0.0001
$2p^3 10s\ ^3S_1$	922.2053(16)	−0.0059	0.0010
$2p^3 7d\ ^3D_3$	929.5154(11)	0.0002	0.0014
$2p^3 6d\ ^3D_3$	936.6278(11)	0.0000	0.0017
	J1358 + 6522		
$2p^3 9d\ ^3D_3$	921.8652(27)	−0.0129	0.0047
$2p^3 8d\ ^3D_2$	924.9615(21)	−0.0131	0.0017
$2p^3 4d\ ^3D_3$	971.7397(6)	−0.0002	−0.0015
$2p^3 5s\ ^3S_1$	976.4490(9)	−0.0003	−0.0007
$2p^3 3s'\ ^3D_3$	988.7728(6)	−0.0006	0.0007
$2p^3 3s'\ ^3D_2$	988.6560(5)	−0.0001	−0.0010
$2p^3 3s'\ ^3D_1$	988.5754(30)	0.0002	0.0024
$2p^3 4s\ ^3S_1$	1039.2311(6)	−0.0004	−0.0007
$2p^3 3s\ ^3S_1$	1302.1684(6)	−0.0005	0.0001

Note. The transitions all originate from the ground state $2p^4\ ^3P_2$ with the upper state indicated in the first column. The astrophysical data are corrected for the observed redshift z. Values in units of angstroms.

precision, we suspected that the discrepancy may be due to the poorly determined O I laboratory wavelengths, which were available prior to the work reported here. Indeed, the O I VUV absorption lines in the various databases (Moore 1993; Morton 2003; Kramida et al. 2020) all rely on the data in Huffman's study from 1967 (Huffman et al. 1967a, 1967b), which were determined with an accuracy limited to $\sim$2 cm^{-1}. In Table 10 a comparison is made for the absorption features in J0814+5029 and J1358+6522 based on the old UV database and the new VUV-FTS data presented in this paper. As can be seen in Figure 12 showing spectral portions of J0814+5029, this apparent discrepancy has now been resolved by the new

laboratory measurements presented here. In particular, those transitions to the 8*d*, 9*d*, and 12*d* levels in Table 10, which used to have differences of > 0.01 Å with the NIST database are now consistent with the present lab measurements. Overall, there is now an excellent agreement between the astrophysical and present laboratory determination of the D I and O I rest wavelengths (all within 2σ).

The reported measurements of the ^{16}O–^{18}O isotope shifts may also be relevant to astronomical studies. The astronomical measurement of isotope ratios can provide important clues to the stellar nucleosynthesis of the elements (Welsh et al. 2020). The largest isotope shifts are observed for the $2p^4\ ^3P_J$—$2s2p^5$ $^3P_{J'}$ transitions at around 792 Å, where the isotope shift of $\sim 0.79\ \mathrm{cm}^{-1}$ translates to a velocity shift of 1.9 km s^{-1}. Unfortunately, the wavelength of this transition is below the limit of the Lyman series of neutral hydrogen at 912 Å; in this wavelength regime the universe is opaque even over short path lengths (Jenkins et al. 2000). For transitions at wavelengths longer than the Lyman limit, the ^{16}O–^{18}O isotope shifts are less than 1 km s^{-1}, making the detection of ^{18}O absorption very challenging.

5. Conclusion

Transition frequencies of some 208 VUV transitions of atomic oxygen were measured at a relative accuracy of 3×10^{-7} by Fourier-transform VUV spectroscopy at the SOLEIL synchrotron facility. Based on the new measurements a global reanalysis of O I level energies was performed, where also the precision VUV-laser spectroscopic data (Ivanov et al. 2008) and the data in the visible domain from Eriksson and coworkers (Eriksson & Isberg 1963, 1964; Eriksson 1965; Eriksson & Isberg 1968; Isberg 1968) were included. As a result it leads to a comprehensive set of improved recommended level energies, which can in turn improve the present NIST atomic database (Kramida et al. 2020). While transitions with longer wavelengths that involve states with $n \leqslant 7$ at excitation energies below 108,000 cm^{-1} are in good agreement with the data in the NIST database, this agreement does not hold for transitions involving levels with $n > 7$ at excitation energies above 108,000 cm^{-1}. The transition-level energies for $n > 7$ in the NIST database were adopted and derived from the study by Huffman and coworkers in 1967 (Huffman et al.

1967a, 1967b) at limited accuracy. Also a comparison was made with the recent comprehensive data set of Civiš and coworkers obtained from infrared spectroscopy (Civiš et al. 2018). Apart from the known levels based on literature there are only six levels that overlap between the present data set and that of Civiš et al. (2018), and those levels are in agreement. With the present study and that of Civiš and coworkers (Civiš et al. 2018), there now exist two complementary resources for the level structure of O I. From the combination of the two a comprehensive database of recommended lines and levels can be formed that improves and extends the presently available NIST database, often used in the spectroscopic and astronomical community.

The ^{18}O isotopic shifts were measured for the first few members of the normal term series, which are compared to quantum calculations (Jönsson & Godefroid 2000). The accurate laboratory wavelengths in this study will be a useful resource to the calibration of the highest resolution astronomical spectra, such as the example application of high-redshift absorbers presented here.

Appendix

The result of a least-squares optimization for extracting the level energies of O I through the LOPT program (Kramida 2011) is tabulated in Table 11. The presented level energies and uncertainties are relative to the lowest-lying $2p^4$ $^3P_2$ state. Note that this level list pertains only to the main ^{16}O isotope of oxygen. In Table 11 a comparison is made with the NIST database of level energies (Kramida et al. 2020).

Table 11
Extracted Level Energies for ^{16}O from an LOPT Analysis

Level	This Work	NIST	Difference
$^3P_2$	0	0	0.000
$^3P_1$	158.268741(5)[a]	158.265	0.004
$^3P_0$	226.985246(6)[a]	226.977	0.008
$^1D_2$	15867.864(4)	15,867.862	0.002
$3s\,^3S_1$	76,794.977(20)	76,794.978	−0.001
$4s\,^3S_1$	96,225.038(20)	96,225.049	−0.011
$3d\,^3D_1$	97,488.369(5)[b]	97,488.378	−0.009
$3d\,^3D_2$	97,488.429(6)[b]	97,488.448	−0.019
$3d\,^3D_3$	97,488.531(8)[b]	97,488.538	−0.008
$3s'\,^3D_3$	101,135.394(8)[b]	101,135.407	−0.013
$3s'\,^3D_2$	101,147.517(6)[b]	101,147.526	−0.009
$3s'\,^3D_1$	101,155.411(20)	101,155.422	−0.011
$5s\,^3S_1$	102,411.978(5)[b]	102,411.995	−0.017
$3s'\,^1D_2$	102,662.056(35)	102,662.026	0.030
$4d\,^3D_3$	102,908.382(8)[b]	102,908.374	0.008
$4d\,^3D_2$	102,908.449(6)[b]	102,908.443	0.006
$4d\,^3D_1$	102,908.497(5)[b]	102,908.489	0.008
$6s\,^3S_1$	105,165.211(5)[b]	105,165.232	−0.021
$5d\,^3D_2$	105,409.002(8)	105,409.008	−0.006
$5d\,^3D_1$	105,409.009(8)	105,409.008	0.001
$5d\,^3D_3$	105,409.010(8)	105,409.008	0.002
$7s\,^3S_1$	106,627.926(35)	106,627.934	−0.008
$6d\,^3D_1$	106,765.800(59)	106,765.803	−0.003
$6d\,^3D_2$	106,765.801(38)	106,765.803	−0.002
$6d\,^3D_3$	106,765.804(39)	106,765.803	0.001
$8s\,^3S_1$	107,497.200(25)	107,497.224	−0.024
$7d\,^3D_1$	107,582.747(27)	107,582.777	−0.030
$7d\,^3D_2$	107,582.763(47)	107,582.777	−0.014
$7d\,^3D_3$	107,582.778(39)	107,582.777	0.001
$9s\,^3S_1$	108,055.637(35)	108,056.0	−0.363
$8d\,^3D_1$	108,112.376(30)	108,114.0	−1.624
$8d\,^3D_2$	108,112.392(38)	108,114.0	−1.608
$8d\,^3D_3$	108,112.415(39)	108,114.0	−1.585
$10s\,^3S_1$	108,435.611(35)	108,436.3	−0.689
$9d\,^3D_1$	108,475.181(49)	108,476.7	−1.519
$9d\,^3D_1$	108,475.181(35)	108,476.7	−1.519
$9d\,^3D_2$	108,475.182(49)	108,476.7	−1.518
$11s\,^3S_1$	108,705.792(35)	108,705.5	0.292
$10d\,^3D_1$	108,734.431(29)	108,736.1	−1.669
$10d\,^3D_3$	108,734.455(49)	108,736.1	−1.645
$10d\,^3D_2$	108,734.458(35)	108,736.1	−1.642
$12s\,^3S_1$	108,904.695(35)	108,906.1	−1.405
$11d\,^3D_3$	108,926.160(49)	108,927.2	−1.040
$11d\,^3D_2$	108,926.174(35)	108,927.2	−1.026
$11d\,^3D_1$	108,926.188(49)	108,927.2	−1.012
$13s\,^3S_1$	109,055.364(35)	109,056.0	−0.636
$12d\,^3D_1$	109,071.895(49)	109,073.3	−1.405
$12d\,^3D_2$	109,071.896(35)	109,073.3	−1.404
$12d\,^3D_3$	109,071.897(49)	109,073.3	−1.403
$14s\,^3S_1$	109,172.358(35)	109,171.7	0.658
$13d\,^3D_1$	109,185.243(49)	109,186.3	−1.057
$13d\,^3D_2$	109,185.259(35)	109,186.3	−1.041
$13d\,^3D_3$	109,185.275(49)	109,186.3	−1.025
$15s\,^3S_1$	109,264.869(35)	109,265.9	−1.031
$14d\,^3D_2$	109,275.149(49)	109,278.2	−3.051
$14d\,^3D_3$	109,275.149(49)	109,278.2	−3.051
$16s\,^3S_1$	109,339.285(35)	109,341.0	−1.715
$15d\,^3D_3$	109,347.675(49)	109,348.9	−1.225
$15d\,^3D_2$	109,347.683(35)	109,348.9	−1.217
$15d\,^3D_1$	109,347.691(49)	109,348.9	−1.209
$16d\,^3D_2$	109,407.001(49)	109,409.5	−2.499
$16d\,^3D_3$	109,407.001(49)	109,409.5	−2.499
$17d\,^3D_2$	109,456.187(49)	109,457.6	−1.413
$17d\,^3D_3$	109,456.187(49)	109,457.6	−1.413
$3s''\,^3P_2$	113,910.937(25)	113,910.957	−0.020
$3s''\,^3P_1$	113,921.370(20)	113,921.391	−0.021
$3s''\,^3P_0$	113,927.520(35)	113,927.534	−0.014
$3s''\,^1P_1$	115,918.118(35)	115,918.143	−0.025
$4s'\,^3D_3$	122,420.0(5)	122,419.7	0.3
$4s'\,^1D_2$	122,797.630(35)	122,797.661	−0.031
$3d'\,^3P_2$	123,296.780(25)	123,296.777	0.003
$3d'\,^3P_1$	123,355.561(25)	123,355.512	0.049

Table 11
(Continued)

Level	This Work	NIST	Difference
$3d'\,^1D_2$	124,319.101(35)	124,319.175	−0.074
$3d'\,^1F_3$	124,326.760(35)	124,326.779	−0.019
$2s2p^5\,^3P_2$	126,266.901(25)	126,266.896	0.005
$2s2p^5\,^3P_1$	126,340.242(20)	126,340.225	0.017
$2s2p^5\,^3P_0$	126,383.776(35)	126,383.751	0.025
$5s'\,^3D_3$	128,979.212(35)	128,978.8	0.412
$5s'\,^1D_2$	129,132.338(35)	129,132.323	0.015
$4d'\,^3D_3$	129,689.7(5)	129,692.3	−2.6
$4d'\,^3S_1$	129,736.6(2)	129,736.6	0.0
$4d'\,^3P_2$	129,970.027(25)	129,970.000	0.027
$4d'\,^3P_1$	129,979.398(20)	129,979.384	0.014
$4d'\,^3P_0$	129,984.589(35)	129,984.553	0.036
$6s'\,^3D_3$	131,855.294(35)	131,854.5	0.794
$6s'\,^3D_2$	131,865.758(25)	131,865.5	0.258
$6s'\,^1D_2$	131,935.763(35)	131,936	−0.237
$5d'\,^3D_3$	132,194.973(35)	132,203.4	−8.427
$5d'\,^1P_1$	132,205.256(35)	132,203	2.256
$5d'\,^1D_2$	132,230.925(35)	132,240	−9.075
$5d'\,^3S_1$	132,233.542(33)	132,232.6	0.942
$5d'\,^1D_2$	132,236.446(35)	132,235	1.446
$5d'\,^3P_2$	132,310.519(25)	132,311.1	−0.581
$5d'\,^3P_1$	132,316.125(20)	132,316.2	−0.075
$5d'\,^3P_0$	132,318.658(35)		
$7s'\,^3D_3$	133,370.215(35)	133,369.8	0.415
$7s'\,^3D_2$	133,379.709(33)	133,378.8	0.909
$6d'\,^3D_3$	133,561.905(35)	133,566.8	−4.895
$6d'\,^3D_2$	133,566.294(35)	133,566.8	−0.506
$6d'\,^1P_1$	133,569.174(35)	133,569	0.174
$6d'\,^3S_1$	133,578.530(35)	133,577.9	0.630
$6d'\,^1D_2$	133,588.032(35)	133,587	1.032
$6d'\,^3P_2$	133,622.115(25)	133,622.0	0.115
$6d'\,^3P_1$	133,626.881(20)	133,626.5	0.381
$6d'\,^3P_0$	133,628.502(35)		
$8s'\,^3D_3$	134,265.424(35)	134,265.3	0.124
$8s'\,^3D_2$	134,273.561(35)	134,273.4	0.161
$7d'\,^3D_3$	134,384.100(35)	134,385.0	−0.900
$7d'\,^3D_2$	134,387.443(35)	134,385.0	2.443
$7d'\,^1P_1$	134,389.480(35)	134,387	2.480
$7d'\,^3S_1$	134,398.555(35)	134,402.5	−3.945
$7d'\,^1D_2$	134,405.663(35)	134,409	−3.337
$7d'\,^3P_2$	134,421.934(25)	134,421.4	0.534
$7d'\,^3P_1$	134,425.901(20)	134,426.5	−0.599
$7d'\,^3P_0$	134,426.548(35)		
$9s'\,^3D_3$	134,838.192(35)	134,839.0	−0.808
$8d'\,^3D_3$	134,916.743(35)	134,919.2	−2.457
$8d'\,^3D_2$	134,919.174(35)	134,919.2	−0.026
$8d'\,^1P_1$	134,920.742(35)	134,921	−0.258
$8d'\,^3S_1$	134,926.643(35)	134,919.2	7.443
$8d'\,^3P_2$	134,944.996(25)	134,943.8	1.196
$8d'\,^3P_1$	134,947.669(20)	134,947.1	0.569
$10s'\,^3D_3$	135,226.729(35)	135,226.7	0.029
$9d'\,^3D_3$	135,281.413(35)	135,283.7	−2.287
$9d'\,^3D_2$	135,283.132(35)	135,283.7	−0.568
$9d'\,^1P_1$	135,284.237(35)	135,285	−0.763
$9d'\,^3S_1$	135,287.096(35)	135,283.7	3.396
$9d'\,^3P_2$	135,305.416(25)	135,303.5	1.916
$9d'\,^3P_1$	135,306.776(25)	135,305.0	1.776
$11s'\,^3D_3$	135,502.317(35)	135,502.3	0.017
$10d'\,^1P_1$	135,541.830(35)	135,542	−0.170
$10d'\,^3D_3$	135,542.831(35)	135,541.7	1.131
$10d'\,^3D_2$	135,544.110(35)	135,541.7	2.410
$10d'\,^3S_1$	135,544.556(35)	135,541.7	2.856
$10d'\,^3P_2$	135,563.574(35)	135,560.3	3.274
$10d'\,^3P_1$	135,563.782(25)	135,562.2	1.582
$12s'\,^3D_3$	135,704.808(35)	135,701.8	3.008
$11d'\,^3S_1$	135,733.090(35)	135,732.4	0.690
$11d'\,^3D_3$	135,734.868(35)	135,732.4	2.468
$11d'\,^3D_2$	135,735.971(35)	135,732.4	3.571
$11d'\,^3P_1$	135,753.9(3)	135,751.7	2.2
$11d'\,^3P_2$	135,754.533(35)	135,752.9	1.633
$12d'\,^3S_1$	135,876.417(35)	135,876.4	0.017
$12d'\,^3D_3$	135,877.446(35)	135,876.4	1.046

Table 11
(Continued)

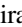| Level	This Work	NIST	Difference
$13d'$ $^3S_1$	135,986.501(35)	135,986.4	0.101
$13d'$ $^3D_3$	135,988.295(35)	135,986.4	1.895
$14d'$ $^3S_1$	136,071.238(35)	136,071.3	−0.062
$14d'$ $^3D_3$	136,073.778(35)	136,071.3	2.478
$15d'$ $^3S_1$	136,137.057(35)	136,138.9	−1.843
$16d'$ $^3S_1$	136,192.498(35)	136,194.4	−1.902
$16d'$ $^3D_3$	136,195.729(35)	136,194.4	1.329
$3d''$ $^3P_0$	137,958.434(35)	137,946.5	11.934
$3d''$ $^3P_1$	137,959.780(35)	137,946.5	13.280
$3d''$ $^3P_2$	137,963.591(25)	137,946.5	17.091
$4d''$ $^3P_1$	143,364.2(2)[c]	143,363.4	0.8
$4d''$ $^3P_2$	143,365.3(1)[c]	143,363.4	1.9
$5d''$ $^3P_2$	145,870.0(2)[c]	145,870.5	−0.5
$6d''$ $^3P_0$	147,228.5(2)[c]	147,230.1	−1.6
$6d''$ $^3P_2$	147,230.1(1)[c]	147,,230.1	0.0
$7d''$ $^3P_0$	148,047.2(2)[c]	148,047.7	−0.6
$7d''$ $^3P_2$	148,048.6(1)[c]	148,047.7	0.9
$8d''$ $^3P_0$	148,577.9(2)[c]	148,576.9	1.0
$8d''$ $^3P_2$	148,579.2(1)[c]	148,576.9	2.3
$9d''$ $^3P_2$	148,941.4(2)[c]	148,945.4	−4.0
$9d''$ $^3P_1$	148,942.9(2)[c]	148,945.4	−2.5
$10d''$ $^3P_2$	149,201.3(2)[c]	149,200.6	0.7
$10d''$ $^3P_1$	149,202.7(2)[c]	149,200.6	2.1
$11d''$ $^3P_1$	149,393.3(3)[c]	149,390.6	2.7
$11d''$ $^3P_2$	149,393.3(3)[c]	149,390.6	2.7
$12d''$ $^3P_2$	149,539.0(2)[c]	149,539.4	−0.4
$12d''$ $^3P_1$	149,540.7(2)[c]	149,539.4	1.3
$13d''$ $^3P_1$	149,652.5(3)[c]	149,652.2	0.3
$13d''$ $^3P_2$	149,652.5(3)[c]	149,652.2	0.3
$14d''$ $^3P_1$	149,742.5(3)[c]	149,744.9	−2.4
$14d''$ $^3P_2$	149,742.5(3)[c]	149,744.9	−2.4

Notes. Values in units of cm^{-1}.
[a] Zink et al. (1991); De Natale et al. (1993).
[b] Ivanov et al. (2008).
[c] Tentative assignment.

ORCID iDs

W. Ubachs https://orcid.org/0000-0001-7840-3756
R. Cooke https://orcid.org/0000-0001-7653-5827
M. Pettini https://orcid.org/0000-0002-5139-4359
N. de Oliveira https://orcid.org/0000-0001-7828-7206
E. J. Salumbides https://orcid.org/0000-0002-1903-146X

References

Bahcall, J. N., & Schmidt, M. 1967, PhRvL, 19, 1294
Brown, J. M., Evenson, K. M., & Zink, L. R. 1993, PhRvA, 48, 3761
Brown, P., Davies, P., & Johnson, S. 1987, CPL, 133, 239
Brown, R. A. 1981, ApJ, 244, 1072
Chang, E. S., Barowy, W. M., & Sakai, H. 1988, PhyS, 38, 22
Civiš, S., Kubelík, P., Ferus, M., et al. 2018, ApJS, 239, 11
Conway, R., Meier, R., & Huffman, R. 1988, P&SS, 36, 963

Cooke, R., & Pettini, M. 2016, MNRAS, 455, 1512
Cooke, R. J., Pettini, M., & Jorgenson, R. A. 2015, ApJ, 800, 12
Cooke, R. J., Pettini, M., Jorgenson, R. A., Murphy, M. T., & Steidel, C. C. 2014, ApJ, 781, 31
De Natale, P., Bellini, M., Goetz, W., Prevedelli, M., & Inguscio, M. 1993, PhRvA, 48, 3757
de Oliveira, N., Joyeux, D., Roudjane, M., et al. 2016, J. Synchrotron Radiat., 23, 887
de Oliveira, N., Roudjane, M., Joyeux, D., et al. 2011, NaPho, 5, 149
Dehmer, P. M., Luken, W. L., & Chupka, W. A. 1977, JChPh, 67, 195
Edlén, B. 1943, Kungl. Svenska Vetenskapsakad. Handl, 20, 3
Eikema, K. S. E., Ubachs, W., & Hogervorst, W. 1994, PhRvA, 49, 803
Eriksson, K. B. 1965, Ark. f. Fysik, 30, 199
Eriksson, K. B., & Isberg, H. B. S. 1963, Ark. f. Fysik, 24, 549
Eriksson, K. B., & Isberg, H. B. S. 1964, Ark. f. Fysik, 26, 247
Eriksson, K. B., & Isberg, H. B. S. 1968, Ark. f. Fysik, 37, 221
Ernst, K., Minutolo, P., Sasso, A., Tino, G. M., & Inguscio, M. 1989, OptL, 14, 554
Field, G. B., & Steigman, G. 1971, ApJ, 166, 59
Gianfrani, L., Sasso, A., Tino, G. M., & Inguscio, M. 1990, OptCo, 78, 158
Hébrard, G., & Moos, H. W. 2003, ApJ, 599, 297
Herzberg, G. 1958, RSPSA, 248, 309
Hopfield, J. J. 1924, ApJ, 59, 114
Hopfield, J. J. 1931, PhRv, 37, 160
Huffman, R. E., Larrabee, J. C., & Tanaka, Y. 1967a, JChPh, 46, 2213
Huffman, R. E., Larrabee, J. C., & Tanaka, Y. 1967b, JChPh, 47, 4462
Isberg, H. B. S. 1968, Ark. f. Fysik, 35, 495
Ivanov, T. I., Salumbides, E. J., Vieitez, M. O., et al. 2008, MNRAS, 389, L4
Jenkins, E. B., Oegerle, W. R., Gry, C., et al. 2000, ApJL, 538, L81
Jönsson, P., & Godefroid, M. R. 2000, MolPh, 98, 1141
Keller-Rudek, H., Moortgat, G. K., Sander, R., & Sörensen, R. 2013, ESSD, 5, 365
Kotuš, S. M., Murphy, M. T., & Carswell, R. F. 2017, MNRAS, 464, 3679
Kramida, A., Yu, R., Reader, J. & NIST ASD Team 2020, NIST Atomic Spectra Database (v5.8) (Gaithersburg, MD: National Institute of Standards and Technology), https://physics.nist.gov/asd
Kramida, A. E. 2011, CoPhC, 182, 419
Lai, K.-F., Ubachs, W., De Oliveira, N., & Salumbides, E. 2020, Atoms, 8, 62
Lurie, J. B., & Baird, J. C. 1986, CPL, 125, 389
Marin, F., Fort, C., Prevedelli, M., et al. 1993, ZPhyD, 25, 191
Marinov, D., Booth, J.-P., Drag, C., & Blondel, C. 2017, JPhB, 50, 065003
McKay, A. J., Chanover, N. J., Morgenthaler, J. P., et al. 2012, Icar, 220, 277
Mercier, B., Compin, M., Prevost, C., et al. 2000, JVST, 18, 2533
Moore, C. E. 1993, in Tables of Spectra of Hydrogen, Carbon, Nitrogen, and Oxygen Atoms and Ions, ed. J. W. Gallagher (Boca Raton, FL: CRC Press), 339
Morton, D. C. 2003, ApJS, 149, 205
Parker, L. W., & Holmes, J. R. 1953, JOSA, 43, 103
Runge, C., & Paschen, F. 1896, ApJ, 4, 317
Runge, C., & Paschen, F. 1897, AnPhy, 297, 641
Runge, C., & Paschen, F. 1898, ApJ, 8, 70
Savin, D. W. 2002, ApJL, 566, 599
Stewart, A. I. F., Alexander, M. J., Meier, R. R., et al. 1992, JGRA, 97, 91
Taubenberger, S., Kromer, M., Pakmor, R., et al. 2013, ApJL, 775, L43
Welsh, L., Cooke, R., Fumagalli, M., & Pettini, M. 2020, MNRAS, 494, 1411
Western, C. M., Booth, J.-P., Chatterjee, A., & de Oliveira, N. 2020, MolPh, 119, e1741714
Wolfe, A. M., Gawiser, E., & Prochaska, J. X. 2005, ARA&A, 43, 861
Zimmerman, M. L., Littman, M. G., Kash, M. M., & Kleppner, D. 1979, PhRvA, 20, 2251
Zink, L. R., Evenson, K. M., Matsushima, F., Nelis, T., & Robinson, R. L. 1991, ApJL, 371, L85